

PARCELY: A Particle-Resolved Cloud Parcel Model With Condensed- and Gas-Phase Organic Aerosol Treatment

Dan Barthaux

Department of Atmospheric and Oceanic Sciences
McGill University, Montreal
July 2023

A thesis submitted to McGill University in partial fulfillment of the
requirements of the degree of Master of Science

©Dan Barthaux, 2023

Contents

1	Introduction and Background	1
2	Model	6
2.1	Theory and Description of the PARCELY Model	6
2.1.1	Domain and Droplet Dynamics	8
2.1.2	Thermodynamic Parameters	9
2.1.3	Co-condensation and Organic Treatment	10
2.1.4	Determining Activation	13
2.1.5	Numerical Details	14
2.2	Internal Error Estimation From Variability	14
2.3	Validation	18
3	Sensitivity Analyses	21
3.1	Impact of Accommodation Coefficients	21
3.1.1	Motivation	21
3.1.2	Results	23
3.1.3	Discussion	30
3.2	Heterogeneous Ambient Fields	32
3.2.1	Motivation	32
3.2.2	Results	34
3.2.3	Discussion	40
4	Results: Co-condensation and Organic Films	42
5	Conclusions	52
6	Future Work	54
7	References	55
8	Appendix	63

Acknowledgements

I would first like to thank my supervisor, Prof. Andreas Zuend, for his help and guidance throughout my master's research. He was especially patient and allowed me to explore multiple avenues of research, while still keeping me on track for the main theme of the project. His comments and improvements to my manuscripts, abstracts, and figures were always abundant and constructive, and helped me achieve better standards of writing and presentation. His assistance and expertise in numerical problems and the use of the AIOMFAC model was especially appreciated.

I would also like to thank the PhD students in Prof. Zuend's group, Ryan and Camilo, who took the time to help me with various issues or questions I would consistently pester them with. I would like to thank the administrative and I.T. staff of the department for their constant assistance since my first day at McGill University.

Finally, I would like to thank my friends and family, who have readily listened to my incessant complaints about coding errors without complaints of their own. Their support and affirmations are always there when I need them.

Abstract

There are many cloud parcel models currently in use for the modelling and subsequent parameterization of cloud microphysics in climate and weather models. Bulk and bin models are efficient and computationally inexpensive, yet lack the resolution and detail of their Lagrangian counterparts such as Direct Numerical Simulation (DNS) or super-droplet models, which can be prohibitively expensive to run. A particle-resolved cloud parcel model, PARCELY, is presented in this thesis. It includes the treatment of organic aerosols via co-condensation and organic-films, which up until now have not been included simultaneously in any public parcel model. Selected simulations show that the combination of both co-condensation and the depression of droplet surface tension by organic-films further increases the amount of activated droplets than either effect by itself, but is highly variable on updraft velocity, organic vapor concentration, and aerosol size distribution. In addition, sensitivity analysis on the mass and thermal accommodation coefficients present in the adjusted terms for diffusivity of water vapor and thermal conductivity of air shows that the choice of values has important ramifications for the peak supersaturation, and that the thermal coefficient is the dominant of the two. Finally, PARCELY is extended to a three-dimensional model to test the impact of spatial inhomogeneity in environmental supersaturation on droplet growth in volumes less than 10 cubic centimeters. The profile of standard deviation of supersaturation from a complex DNS model is qualitatively reproduced with unrealistic droplet dynamics even in such volumes, and droplet dynamics is shown to be a major factor in the ambient supersaturation, adding to the known importance of turbulence in cloud microphysics.

Abrégé

Il existe de nombreux modèles de parcelles de nuages actuellement utilisés pour la modélisation et la paramétrisation subséquente de la microphysique des nuages dans les modèles climatiques et météorologiques. Les modèles en vrac et bin sont efficaces et peu coûteux en calcul, mais n'ont pas la résolution et le détail de leurs homologues Lagrangiens tels que la simulation numérique directe (DNS) ou les modèles de super-gouttelettes, qui peuvent être d'un coût prohibitif à exécuter. Un modèle de parcelle de nuage résolu en particules, PARCELY, est présenté dans cette thèse. Il comprend le traitement des aérosols organiques par co-condensation et des films organiques, qui jusqu'à présent n'étaient inclus simultanément dans aucun modèle de parcelles public. Des simulations sélectionnées montrent que la combinaison de la co-condensation et de la dépression de la tension superficielle des gouttelettes par les films organiques augmente davantage la quantité de gouttelettes activées que l'un ou l'autre effet par eux-mêmes, mais est très variable sur la vitesse de courant ascendant, la concentration de vapeur organique, et la distribution de la taille des aérosols. De plus, l'analyse de sensibilité sur les coefficients d'accommodation massique et d'accommodation thermique présents dans les termes ajustés de diffusivité de la vapeur d'eau et de conductivité thermique de l'air montre que le choix des valeurs a des ramifications importantes pour le pic de sursaturation, et que le coefficient d'accommodation thermique est le facteur dominant des deux. Enfin, PARCELY est étendu à un modèle tridimensionnel pour tester l'impact de l'inhomogénéité spatiale dans la sursaturation environnementale sur la croissance des gouttelettes dans des volumes moins de 10 centimètres cubes. Le profil de l'écart type de sursaturation à partir d'un modèle DNS complexe est reproduit qualitativement avec une dynamique de gouttelettes irréaliste, même dans de tels volumes, et la dynamique des gouttelettes s'avère être un facteur majeur dans la sursaturation ambiante, ajoutant à l'importance connue de la turbulence dans la microphysique des nuages.

Thesis Structure and Author Contributions

This thesis is comprised of several chapters. Chapter 1 serves as a literature review and introduction to the theory and requirements for the development of PARCELY, a new cloud parcel model. Chapter 2 is a detailed presentation of the theory, framework, and numerical approach behind the PARCELY model. Chapter 3 contains the work from sensitivity analyses performed on accommodation coefficients and non-homogeneous ambient variables for their affects on droplet activation and the evolution of aerosols in a cloud, including motivations for these tests and discussions. Chapter 4 presents the results of experiments using PARCELY accounting for co-condensation and organic films, and how they affect droplet activation. Chapter 5 contains conclusions of the experiments and the model as a whole. Chapter 6 is the final section dedicated to potential future uses of the PARCELY model and possible future work to follow up on the experiments described herein.

I created and coded the entirety of the PARCELY model, generated all of the data, and performed the research and writing for the thesis. Prof. Andreas Zuend supplied ample guidance on numerical issues, research directions and ideas, validation data (namely from Thomas et al. (in prep) and Topping and Bane, 2022), and instruction or corrections on the writing of the thesis for the duration of my master's degree.

1 Introduction and Background

Clouds are a fundamental and ubiquitous part of Earth’s climate system. Without the water in the atmosphere necessary to form clouds, many phenomena in our lives such as thunderstorms, hurricanes, or blizzards, would not occur. Currently, clouds, their constituents, and their effects on the atmosphere are one of the largest sources of uncertainty in climate and weather models, influencing crucial projections for the future of life on Earth (Bellouin et al., 2020). Many fundamental processes in the life-cycle of a cloud - such as the formation of cloud droplets, precipitation, or ice, and the effects of turbulent features and entrainment or detrainment of air - are still subject to uncertainties and disagreement.

Clouds also have large uncertainties in their radiative effects on the climate system. The effects can be divided into two groups: the direct radiative effect (DRE) and the indirect radiative effect (IRE). The DRE is due to the absorption, scattering, and transmittance of radiation by the aerosols that can act as activation sites on which cloud droplets form, known as cloud condensation nuclei (CCN) (Held et al., 2014). The IRE is commonly separated into the cloud lifetime effect (Lindsey and Fromm, 2008) and the albedo effect (Twomey et al., 1984). Both are dependent on an underpinning aerosol population’s geometric and chemical properties.

To better understand and model clouds throughout their lifetimes, an adequate understanding of aerosols and their impact while serving as cloud condensation nuclei is required. An aerosol is a collection of particulate matter in both solid and liquid phases suspended in a gas (most commonly assumed to be air in atmospheric sciences; Hinds, 1999). In this thesis, “aerosol” is used to refer to the individual solid or liquid particles that act as the nuclei for cloud droplet formation, as is commonly done in the field of atmospheric chemistry. When considering aerosols and their interactions with water, they are also interchangeably referred to as the solute, and the water as the solvent. Aerosols can be weakly or strongly hygroscopic, a measure of how much a chemical species “wants” to take up water when equilibrated at a given relative humidity (RH), depending on their composition, and so can become aqueous solutions even while residing outside of a cloud (or at a RH lower than 100 %), i.e., without needing to become cloud droplets.

Modelling clouds in their entirety is a difficult task. Any model made with that purpose in mind would have to contend with a scale of processes that spans many orders of magnitude (Krueger, 2000). For example, a single cumulus cloud is on the order of 1 km in horizontal extent, and the radii of its aerosol constituents are on the order of several nanometers to micrometers (Rogers and Yau, 1989). In between these length scales, different microphysical and atmospheric processes occur simultaneously. This renders attempts of modelling an entire cloud unfeasible due to the extreme yet necessary computational requirements (Schneider et al., 2017). Therefore, many cloud-resolving models implement parameterizations of the microphysical processes (Morrison et al., 2020). These parameterizations can come from

empirically-derived fits to observations or from parcel models. Parcel models aim to simulate the microphysical processes of individual cloud parcels or a cluster of them (Hsieh et al., 2009). Four major kinds of models have been developed since research into them first began: bulk, bin, super-droplet, and direct-numerical-simulation (DNS) models.

Bulk and bin models were the first to appear due to the limited computational resources of the mid 20th-century. In order to describe the evolution of populations of cloud particles, statistical representations of their distributions and properties were prescribed (Morrison and Pinto, 2006). Governing equations are applied to distribution functions for a feature of the population, typically size (radius) or mass, represented by the effective radius and the liquid water content (LWC) respectively. Bulk models solve these equations with a restricted number of variables and degrees of freedom, and often contend with a closure problem (Khain et al., 2015). This limits bulk models to using idealized and analytical distributions. Bin models discretize the distribution function into a number of bins as function of droplet size, and can handle disordered and variable distributions (Clark, 1973), however they do not solve for individual droplets.

Owing to recent improvements in computational capabilities, DNS models have become more common in various fields of study over the past 20 years (Chen et al., 2020, Kumar et al., 2017, Bhowmick and Iovieno, 2019). This kind of model explicitly tracks the evolution of every particle in a volume of air with a Lagrangian method, as well as the turbulence of the airflow and water vapour field in the domain, with a grid scale resolution often on the order of the Kolmogorov scale (~ 1 mm) or smaller (Wang et al., 2009). This severely constrains the size of the domain that can realistically be simulated within a reasonable time, despite the computing power found today, as even in 1 m^3 there can be $\sim 10^8$ hydrometeors (liquid or solid water particles) present (Morrison et al., 2020). Recently, the super-droplet method (SDM) approach was developed, inspired by modelling of rarefied gas flows (Shima et al., 2007). Instead of solving for every particle in a volume, they are grouped into “super-droplets” with similar attributes (solute mass and water radius) and act as particles. This can be thought of as a course-grain view of a DNS model that solves for every particle. An interaction like collision-coalescence is slightly more involved numerically, but is still based on a probabilistic approach as in DNS models.

Hilding Köhler developed the initial theory of condensational droplet growth on hygroscopic aerosol particles by combining Raoult’s law and the Kelvin effect (Köhler, 1936). While it has gone through improvements and alterations, his equation has been the backbone of condensational growth in the models mentioned above since its introduction. However the equation – specifically the Kelvin or solute effect term – requires knowledge of multiple solute parameters, like the van’t Hoff dissociation factor and the molar mass. Petters and Kreidenweis, 2007 introduced the hygroscopicity parameter κ , that simplifies the way one can approach modelling a population of aerosols by requiring an input of a single parameter that could be determined experimentally rather than an assortment of parameters. It is worth mentioning that while κ is

often considered a constant, studies have shown that it varies with size and RH (Hodas et al., 2016, Rastak et al., 2017).

An important environmental variable that any parcel model evaluates is the water vapour saturation ratio (hereafter saturation ratio). A saturation ratio represents the existent vapour pressure divided by the equilibrium vapour pressure of a substance at a given temperature. This is identical to RH assuming it is similarly defined. The saturation ratio is dependent on the condensational growth of droplets and the updraft velocity. Each aerosol has a critical saturation threshold, where if it is exposed to an environmental saturation ratio at or above this value, it will “activate” and experience rapid condensational growth (Pruppacher et al., 1998). Not every CCN in an ascending air parcel is guaranteed to activate, and the ratio of activated to unactivated aerosols varies depending on the physicochemical and size properties of each aerosol particle individually and as a population, and the environmental conditions, such as updraft velocity, temperature, and pressure (Rogers and Yau, 1989).

Properties of the aerosol population are also consequential, notably the size distribution and the number concentration. Even though the theory of cloud droplet formation is heavily dependent on the aerosols that serve as the foundations for the droplets, current parcel models tend to omit or simplify several atmospheric physicochemical processes that affect the nature of these aerosols (Kolb et al., 2010). The main assumption that represents this simplification is that the physical characteristics of the aerosols are constant, such as their size, density, hygroscopicity, surface tension, and composition. Due to the prominence of these traits in the base cloud physics equations, removing this assumption could markedly alter the results of a parcel model.

In any volume of air containing aerosols, it is highly unlikely that the population is composed of particles containing only one chemical species, i.e. purely ammonium sulfate or purely sodium chloride. Instead, a mixture of different organics and inorganics is likely to be present, from the viewpoint of both the total population and the individual aerosols themselves. To address this, the concept of an aerosol mixing state was introduced by P. Winkler, 1973, where he describes a population residing on a spectrum between internally mixed – meaning all particles have been completely mixed in terms of their chemical compositions and the population is homogeneous (all of equal composition) – and externally mixed, where little to no mixing has occurred and the population is a heterogeneous mixture of particles with different chemical characteristics. Riemer and West, 2013 developed a framework with which one can quantify the amount of mixing that has occurred within an aerosol population. Assumptions in mixing state have been shown to result in errors in CCN activation by up to 100 % (Riemer et al., 2019), and so must be taken into account carefully.

The primary method for an aerosol to possibly change over time (when focusing on cloud droplet formation) is by co-condensation of organic matter onto the original nucleus (Crooks et al., 2018). In much the same way as an aerosol takes up water, other vapours present in the air around it can condense onto and diffuse into the droplet, driven by the thermodynamics

of equilibrium gas–particle (or vapour–liquid) partitioning. Co-condensation has already been shown to have an appreciable impact on droplet growth and activation (Topping et al., 2013). The addition of organic matter naturally increases the total solute mass of a particle, and thus its size, making the droplet more likely to activate. However other effects must be considered due to the change in composition. Namely, the typical hygroscopicities of organics tend to be much lower than those of inorganics (that are often considered as the whole solute in parcel models), which in turn lowers the effective hygroscopicity of the particle. Thus, a particle with more organic content will have a reduced water condensation rate than an equally sized particle with less inorganic content. These two effects (size and hygroscopicity) are seemingly counter-acting, but the net effect is always to increase the likelihood of activation.

Secondly, the introduction of condensed species other than water and preexisting nonvolatile solutes (i.e. the dry particle species) leads to a change in the overall surface tension of the particle (Topping et al., 2007). Most parcel models assume that the surface tension of every particle is equal to the surface tension of pure water, and in some instances ignore the temperature dependence of the surface tension, which can vary by $\sim 10\%$ in the temperature range of a typical cumulonimbus cloud. However once multiple components are considered, such an assumption is incorrect, especially prior to CCN activation; observations and rigorous modelling (Ovadnevaite et al., 2017) have shown that there is a non-negligible change in the particle’s surface tension prior to activation and the subsequent domination of water in the particle. The use of the surface tension of pure water is a fair assumption when the size of the droplet is large and the composition of the droplet is predominantly water, as is expected for a cloud droplet. For CCN or aerosols however, their composition matters when considering condensational growth via water vapour. An aerosol particle can actually be composed of several hundreds of components, present in one or several liquid or solid phases in various morphologies (Song et al., 2013, Shiraiwa et al., 2013, Al-Abadleh, 2022). The characteristics and the processes responsible for the formation and behaviour of aerosol particles throughout their lifetime are the subject of intense research across many fields (for example thermodynamic modelling, field, and laboratory experiments).

When organic compounds condense onto and/or into an aerosol particle, they tend to develop into thin films surrounding the core particle (a form of phase separation) (Davies et al., 2019). This coating affects the effective surface tension of the particle; since little-to-no water molecules reside at the surface, it is instead the organic component’s surface tension that dominates. There are several theoretical models that have been constructed to represent this and similar processes (Vepsäläinen et al., 2022) that vary in their complexity and assumptions. Allowing for an evolving surface tension could affect both supersaturation and activated droplet count, as it can substantially alter the droplet equilibrium water vapour saturation ratio term present in the growth rate equation.

While the chemical composition and evolving hygroscopicity and surface tension are important in cloud droplet activation research and modelling, their implementation is difficult without encountering issues. Resolving the particles at such fine scales would require either a numerical/computational sacrifice or a withdrawal from the number of particles simulated. Thus, we introduce simplifications regarding the aerosol population in our models, such as assuming they are perfect spheres, or neglecting other components besides the core solute altogether. However, the assumptions regarding the effective surface tension of the droplet may conceal many of these underlying simplifications, since it is a function of composition and other factors not resolved in parcel models. As an example, Schmedding and Zuend, 2023 present a rigorous thermodynamic treatment of the microscale processes that go into determining the surface tension of a droplet (that is currently not in any cloud parcel model).

Determining the importance of the chemical composition and droplet surface processes in cloud droplet formation can be a potential avenue to exploring and answering still unresolved issues in the field, such as size-distribution broadening (Chandrakar et al., 2016). Bin cloud parcel models have recently been made or adjusted to address the effects of co-condensation during droplet formation (Jia, 2020, Heikkinen et al., 2023) and surface tension (Lowe et al., 2019), although not yet both. With the rapid advances in computing power and efficiency, creating a Lagrangian cloud parcel model with the inclusion of organics, co-condensation, and organic films can be developed, using an alternate modelling approach that can attempt to combine the benefits of both DNS and bin schemes, as well as κ -Köhler theory. This particle-resolved scheme would allow the exploration of the relations between the chemical and physical processes on a droplet-by-droplet basis without needing to resort to computationally costly methods (Grabowski et al., 2019), or sacrificing potentially significant details lost in bulk or bin models.

In this thesis, a new particle-resolved cloud parcel model – PARCELY - is presented, and is used to analyze the effects of co-condensation and organic-film surface tension effects. The model is limited in scope to addressing the impact of these effects only on droplet activation in warm clouds (no consideration of ice particles or microphysics), and ignores the formation of aerosol particles by coagulation. In addition, collision-coalescence is also neglected in the model. The novelty in PARCELY is in its framework, which allows a more accessible approach to aerosol representation in a cloud parcel model and determination of its properties over time, without resorting to possibly computationally expensive DNS or superdroplet models.

2 Model

2.1 Theory and Description of the PARCELY Model

PARCELY simulates a rising parcel of air with a constant volume containing a population of particles. It solves for the evolution of every individual particle initialized. In the model, a particle consists conceptually of a solute representing the aerosol, and a “shell” of liquid water surrounding it, as pictured in Figure 1. This is a simplified and idealized framework, although one that is commonly used and easy to approach numerically. This is not the case in reality, where particle constituents (often referred to as solutes) are typically homogeneously mixed with the condensed water (assuming no phase separation). Both sections of the particle are assumed to be spherical, and the initial mass of water (m_w , kg), is calculated taking into account the solute mass at its center:

$$m_w = \frac{4\pi}{3} \rho_w (r^3 - r_d^3), \quad (1)$$

where r and r_d are the total and solute (“dry”) radius of the particle (m), and ρ_w (kg m^{-3}) is the density of liquid water. The equilibrium saturation ratio of water vapour over the surface of the droplet is calculated using κ -Köhler theory (Petters and Kreidenweis, 2007):

$$S_{\text{surf}} = \frac{r^3 - r_d^3}{r^3 - r_d^3 (1 - \kappa)} \exp \left(\frac{2 \sigma M_w}{r T R_d \rho_w} \right). \quad (2)$$

The unitless hygroscopicity parameter κ is usually experimentally determined for a specific solute or mixture of solutes (alternatively it can be calculated using a thermodynamic model) and represents the tendency of a solute species to take up water, with values ranging from near-zero to around 1.4, with higher values signifying greater hygroscopicity. σ is the effective surface tension of the particle (J m^{-2}), M_w the molar mass of water (kg mol^{-1}), T is environmental temperature (K), and R_d the specific gas constant for dry air ($\text{J kg}^{-1} \text{K}^{-1}$). The dry parameters of hygroscopicity, density, and molar mass are assumed constant unless considering co-condensation (see section 2.1.3).

The growth of a particle is determined by the mass growth rate equation (kg s^{-1}):

$$\frac{dm_n}{dt} = (4\pi)^{2/3} \left(\frac{3m_n}{\rho_w} \right)^{1/3} \left(\frac{S_{\text{env}} - S_{\text{surf}, n}}{F_K + F_D} \right), \quad (3)$$

where S_{env} is the environmental saturation ratio of water vapour, and F_K and F_D (m s kg^{-1}) are terms representing the effects of heat conduction and molecular diffusion of water vapour:

$$F_K = \left(\frac{L}{R_v T} - 1 \right) \frac{L}{K_n^a T} \quad F_D = \frac{R_v T}{D_n^v e_s(T)}.$$

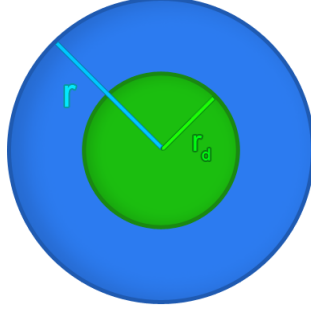


Figure 1: Illustration of an individual particle in the model. r_d is the radius of the dry solute center, and r is the total radius of the particle.

Here R_v is the specific gas constant of water vapour ($\text{J kg}^{-1} \text{K}^{-1}$), L is the latent heat of condensation of water, K_n^a and D_n^v are the kinetic effects-adjusted thermal conductivity of air and the diffusivity of water vapour, respectively, and $e_s(T)$ is the saturation vapour pressure of water vapour at temperature T (further details in section 1.1.1). The equations for the evolution of environmental pressure P (Pa), temperature, and saturation ratio are taken from Rothenberg and Wang, 2017:

$$\frac{dP}{dt} = -\frac{g P W}{R_d T_v}, \quad (4)$$

$$\frac{dT}{dt} = -\frac{g W}{c_p} + \frac{L}{c_p \rho_a} \sum_i^N \frac{dm_n}{dt}, \quad (5)$$

$$\frac{dS_{\text{env}}}{dt} = \left(\frac{L g}{R_v c_p T^2} - \frac{g}{T R_d} \right) W - \left(\frac{P R_v}{R_d e_s(T)} + \frac{L^2}{R_v T^2 c_p} \right) \frac{1}{\rho_a} \sum_i^N \frac{dm_n}{dt}, \quad (6)$$

where g is the gravitational acceleration (m s^{-2}), c_p is the specific heat capacity of air at constant pressure ($\text{J kg}^{-1} \text{K}^{-1}$), and ρ_a is the density of dry air (kg m^{-3}). In Eq.(4), T_v denotes the virtual temperature (K):

$$T_v = T \left(\frac{P + e}{P + \frac{R_d e}{R_v}} \right). \quad (7)$$

The model initializes the aerosol population radii using a seeded random number generator based on a given size distribution. There are three distribution settings: monodisperse, normal, and log-normal, and the number of different solute species is determined via user input. The number concentration is given in particles per cubic centimetre; however, the total number of particles is dependent on the size of the parcel. Increasing the volume of the domain will increase the particle count proportionally, thus keeping the number concentration constant.

The particle wet radius is initially set to their equilibrium radii at the user-defined saturation ratio. Figure 2 shows a representative Köhler curve of an aerosol particle with its respective equilibrium radius for a relative humidity of 96.801%, as well as its critical radius and saturation ratio, which can be used to determine when the droplet activates after a model run. Both the equilibrium radius and the critical parameters are attained by minimizing a form of equation 2 with built-in Python solvers.

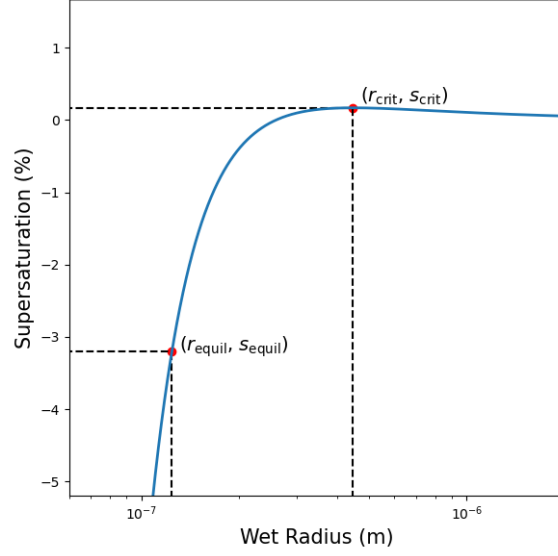


Figure 2: Example of a Köhler curve for a 50 nm (“dry” radius) ammonium sulfate particle at 283 K. The critical and equilibrium radii, r_{crit} and r_{equil} , and their respective supersaturations are marked with the dashed black lines. The ambient saturation ratio is 0.96801.

2.1.1 Domain and Droplet Dynamics

The parcel volume is kept constant for physical and numerical simplicity purposes. We are less interested in how the air expands over time (as is physically realistic) and because we are looking mostly at droplet activation at cloud base with PARCELY, simulations typically do not span large vertical distances, and thus will have small changes in ambient pressure, temperature, or air density. This allows us to assume the effect on the domain volume is minimal, and therefore negligible on the evolution of the hydrometeor population. We still solve for temperature and pressure with prognostic equations (eq. 5 and 6) and air density with a diagnostic equation (eq. 2.1.2).

The particles’ initial vertical velocities are set equal to the updraft velocity. The effects of turbulence are neglected, and air drag is considered only in the vertical direction by assuming that the particles are always falling (relative to zero updraft) at their terminal velocities v_{term} , (m s^{-1}) which are given as

$$v_{\text{term}} = \sqrt{\frac{8 r g (\rho_w - \rho_a)}{3 C_D \rho_a}}. \quad (8)$$

Here C_D is the drag coefficient, which is calculated using a power-law fit to experimental data from Shafrir and Gal-Chen, 1971. Their measurements only begin from radii of 30 μm ; however, the effect of drag on the particles before activation (often below 1 μm) is negligible.

The parcel domain ascends with the median vertical velocity of the particles, which is then used to update the vertical boundaries of the domain. If a non-monodisperse aerosol size distribution is used and droplet activation occurs (typically after $r > 1 \mu\text{m}$ when drag starts to take effect), some droplets will rise more slowly or more rapidly compared to the median; their range of sizes result in a range of terminal velocities (Eq. (8) and thus a range in vertical velocities. We use periodic boundary conditions to address this. Droplets falling out of the domain through the lower boundary reappear at the upper boundary with the same vertical velocity and vice versa.

Collision-coalescence via tracking every particle's position and movement (see sensitivity analysis section on heterogeneous fields) was initially included in the model, but quickly removed due to computational efficiency. In addition, because we are looking at activation of droplets in this thesis, the size range of droplets simulated and the model run-times used would not lead to any meaningful growth or number of collisions (Khain and Pinsky, 2018). The majority of simulations using the basic “billiard-ball” approach of droplet dynamics (further detail in the heterogeneous fields section) in PARCELY resulted in no collisions, which further convinced us that the inclusion of collision-coalescence in this model would not be worthwhile.

2.1.2 Thermodynamic Parameters

Several thermodynamic variables or parameters in this model are allowed to evolve with time using analytical or empirically derived expressions instead of being assumed constant. The latent heat of condensation L (J kg^{-1}) has been parameterized by Rogers and Yau, 1989 as follows:

$$L = (2500.8 - 2.36 T + 0.0016 T^2 - 0.00006 T^3) \times 10^3. \quad (9)$$

For the parameterization above, temperature (T) is given in degrees Celsius. The diffusivity of water vapour ($\text{m}^2 \text{s}^{-1}$) and thermal conductivity of air ($\text{J m}^{-1} \text{s}^{-1} \text{K}^{-1}$) are both adjusted to include kinetic effects (Pruppacher et al., 1998):

$$D^v = 0.211 \left(\frac{T}{T_0} \right)^{1.94} \left(\frac{P_0}{P} \right) \quad (10)$$

$$K^a = (5.69 + 0.017 T) \times 10^{-5} \quad (11)$$

$$D^{v*} = \frac{D_v}{\frac{r}{r+\Delta_v} + \frac{D_v}{r\alpha_c} \left(\frac{2\pi}{R_v T} \right)^{1/2}} \quad (12)$$

$$K^{a*} = \frac{K_a}{\frac{r}{r+\Delta_T} + \frac{K_a}{r\alpha_T c_p \rho_a} \left(\frac{2\pi}{R_d T} \right)^{1/2}} \quad (13)$$

T_0 and P_0 are set to 273.15 K and 1013.25 hPa, Δ_v and Δ_T are vapour and thermal jump lengths (m), and α_c and α_T are the mass and thermal accommodation coefficients. The saturation vapour pressure of water vapour $e_s(T)$ (Pa) is taken from Rogers and Yau, 1989:

$$e_s(T) = e_s^0 \exp \left(\frac{L}{R_v} \left(\frac{1}{283} - \frac{1}{T} \right) \right), \quad (14)$$

with $e_s^0 = 611$ Pa, and the value of L is calculated from Eq. (9). The density of dry air (kg m^{-3}) is calculated using the ideal gas law, using the saturation vapour pressure and saturation ratio to calculate the partial pressure of water vapour (Pa) at a given temperature:

$$\rho_a = \frac{P - e}{R_d T} \quad (15)$$

$$e = e_s S.$$

The surface tension of pure liquid water σ_w (J m^{-2}) is parameterized as a function of temperature (Kalova and Mares, 2018) via

$$\tau = 1 - \frac{T}{T_c},$$

$$\sigma_w = (241.322 \tau^{1.26} (1 - 0.0589 \tau^{0.5} - 0.56917 \tau)) \times 10^{-3}, \quad (16)$$

with the critical temperature (T_c) of water equal to 647.15 K. For $T = 283$ K, this results in a surface tension of 0.0743 J m^{-2} .

2.1.3 Co-condensation and Organic Treatment

In order to update the solute core particle radius, the model assumes that any organic matter condenses directly onto the solute at the center of the nucleus (as illustrated in Figure 1), ignoring any possible interaction with the liquid shell around it. Therefore, the solute variables (mass, radius, density, hygroscopicity) can no longer be considered constant and must be determined at every time-step as well. The mass growth rate equation (kg s^{-1}) for every organic species i and for each of the dry nuclei n is calculated using a similar equation as that for the water growth equation (Eq. 3):

$$\frac{dm_{n,i}}{dt} = 4\pi r_n D_{n,i}^* M_i (C_i - C_{n,i}^{\text{surf}}) N_A^{-1} \quad (17)$$

Here, r_n is the droplet radius (cm) M_i is the molar mass of organic compound i , C_i and $C_{n,i}^{\text{surf}}$ are the vapour concentration and (equilibrium) gas phase concentration at the surface of a particle for the species (in molec cm^{-3}) respectively, N_A is Avogadro's number, and $D_{n,i}^*$ ($\text{cm}^2 \text{s}^{-1}$) is an adjusted diffusivity given by:

$$D_{n,i}^* = \frac{D_i}{\frac{r}{r+0.5 \times 1.12 \times 10^{-7}} + \frac{D_i}{\alpha r} \sqrt{\frac{2\pi M_i}{RT}}}, \quad (18)$$

where α is assumed to be the same value for every organic species and set to 0.1 (Saleh et al., 2013).

The input parameters required for an organic component are density, hygroscopicity (κ), molar mass, surface tension, and saturation vapour concentration (volatility). Alternatively, one can input only volatility and surface tension and have the model determine approximate randomized guesses (within an appropriate range) for the remaining parameters by relying on the volatility basis set framework (VBS) (Donahue et al., 2006, Stolzenburg et al., 2022) and molecular corridor approach (Shiraiwa et al., 2014). For each given volatility, a molar mass is assigned from a uniform sample of values ranging between the bounding lines for linear alkanes and sugar alcohols. Depending on the molar mass' position in between the bounding lines, an oxygen to carbon (O:C) ratio between 0 and 1 is assigned, with low values corresponding to molar masses closer to the upper limit and vice versa. With an O:C ratio, the hydrogen to carbon (H:C) ratio can be approximated (Heald et al., 2010):

$$\text{H:C} = 2 - \text{O:C}, \quad (19)$$

and the density (kg m^{-3}) estimated by (Kuwata et al., 2012):

$$\rho_{\text{org}} = 1000 \frac{12 + \text{H:C} + 16 \text{O:C}}{7 + 5 \text{H:C} + 4.15 \text{O:C}}. \quad (20)$$

Finally, the hygroscopicity parameter is calculated by using a sigmoidal fit by Andreas Zuend (Serrano et al. (in preparation)) as a function of the O:C ratio based on experimental data by Duplissy et al., 2011:

$$\kappa_{\text{org}} = d + \frac{a - d}{(1 + \exp(\text{O:C} - c)^b)^g}, \quad (21)$$

where a , b , c , d , and g are fitted parameters equal to 0, 27, 0.33, 1, and 0.026 respectively. A species' diffusivity in air is estimated by Schnoor et al., 1996 (used in both Lim et al., 2005 and Topping et al., 2013):

$$D_i = 1.9 M_i^{-2/3}, \quad (22)$$

which is a first-order estimation method for gas phase diffusivity applicable in absence of more detailed data or expressions. This expression was chosen solely due to its use in Topping et al.,

2013, which is discussed more in section 4.

The equilibrium gas phase concentration at the surface of an aqueous particle is given by

$$C_{n,i}^{\text{surf}} = \frac{C_i^{\text{sat}} x_{n,i} N_A}{M_i} \exp \left(\frac{2\sigma_n}{RT r_n} \frac{\sum (x_{n,i} M_i)}{\rho_n} \right), \quad (23)$$

where the exponential term is the Kelvin effect, $x_{n,i}$ is the mole fraction of component i in particle n , C_i^{sat} is the saturation vapour concentration of the organic, and the other symbols have their usual meanings. Typically concentration is given in units of $\mu\text{g m}^{-3}$, however molec cm^{-3} is used (due to comparisons for validation with other models). After calculating the new condensed masses of the organics onto each particle core, the mean density and hygroscopicity are recalculated using simple mass-weighted and volume-weighted mixing rules respectively. The effective solute radius is calculated using the new total mass and mean density.

With the introduction of organics, the surface tension of the particle has to be adjusted as well. There are two modes that can be selected: (1) organic film and (2) mixing rule. The latter is another volume-weighted mixing rule based on the particle composition and surface tensions of pure constituents involved, while the former is based off of the simplified organic-film treatment (Ovadnevaite et al., 2017, Davies et al., 2019) in the AIOMFAC model (Zuend et al., 2011). The model assumes that the organic components condense into a thin layer surrounding the entire particle (Ruehl et al., 2016), and the surface tension is then calculated given this organic film is coating a well-mixed aqueous core. However, the organics are also accounted for when calculating the volume of the solute, water content, and overall particle size, and so this approach is an estimation of the actual thermodynamics of the particle.

The organic film treatment starts by calculating the volume (m^3) of the film layer around the particle, assuming the film's thickness, Δ_z , to be roughly the size of a single water molecule (0.3 nm):

$$V_{\text{film}} = \frac{4}{3}\pi(r^3 - (r - \Delta_z)^3).$$

To determine the fraction of organic surface coverage ζ , the individual volumes of organics are summed and compared to the film volume.

$$\zeta = \begin{cases} 1, & \text{if } \frac{\sum V_{\text{org}}}{V_{\text{film}}} \geq 1 \\ \frac{\sum V_i^{\text{org}}}{V_{\text{film}}}, & \text{otherwise.} \end{cases} \quad (24)$$

Finally, the effective surface tension (J m^{-2}) is obtained by

$$\sigma_{\text{eff}} = \zeta \frac{\sum (\sigma_i V_i^{\text{org}})}{\sum V_i^{\text{org}}} + (1 - \zeta) \sigma_w. \quad (25)$$

Because of the difference in mass or density properties in components, an aerosol consisting

of purely an inorganic solute (e.g., ammonium sulphate) will not have the same radius as an aerosol where half of the inorganic solute is replaced with an organic, which would likely have a lower density. In order to maintain the initial CCN size distribution input after taking into account organic components, the model approximates the amount of mass of each solute component (inorganic and organics) required to form a CCN of a pre-determined radius (i.e., the original size distribution) from a user-inputted array of mass fractions for each solute component.

It does so by first calculating the mean density (kg m^{-3}) of the particle:

$$\rho_{\text{mean}} = \sum_i \rho_i w_i, \quad (26)$$

where ρ_i is the density of each solute species i (inorganic and organic), and w_i is the mass fraction. The total mass of the particle is calculated using the mean density, and then the mass of each component found using the mass fraction and the calculated total mass. This approach leads to variations in condensed, vapour, or total organic content when one changes the inorganic solute mass fractions even if the size distribution is the same, as can be seen in Fig. (3). In addition, changes in proportions of composition expected due to the Kelvin effect are ignored when initial particle composition is setup, but the model will then allow for such effects to change the solute composition over time (if co-condensation is enabled).

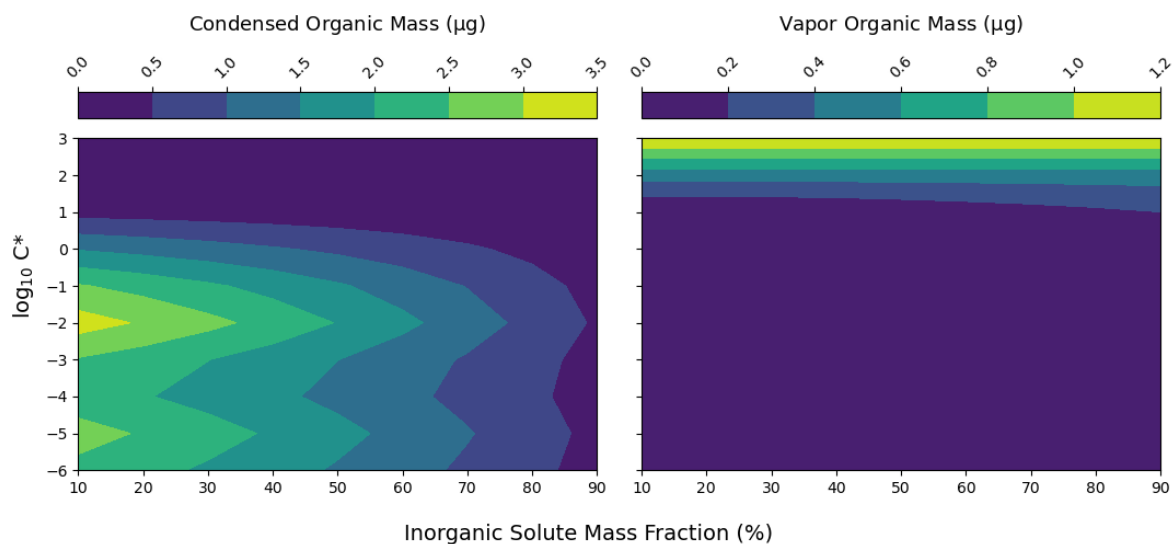


Figure 3: An example of how condensed (left) and vapour (right) content of organics changes with inorganic solute mass fraction. The y-axis is \log_{10} of the saturation concentration of each organic component (a measure of its volatility). The aerosol size distribution used is from Topping et al., 2013 (detailed in the results section).

2.1.4 Determining Activation

Köhler theory posits that a droplet activates once the environment is either supersaturated above the droplet's critical saturation ratio for a reasonably long time (typically several tens of sec-

onds), and subsequently the droplet has grown well beyond its critical radius; this is when the droplet experiences “runaway growth” until it reaches a new dynamic equilibrium state with the environment (Seinfeld and Pandis, 2016). These critical parameters are easy to determine when the solute variables are constant, i.e. the only variable is the wet particle radius. Once composition becomes a factor - either only via surface tension or all the effects of co-condensation - the critical parameters necessarily change with each time step as well. Therefore, applying a constant threshold for either supersaturation or wet radius in such cases is not the most appropriate.

For this reason, we have approached the determination of activation in a simplified and graphical manner. A simple k-means clustering function is applied to the final time-step in the data to sort between activated and unactivated droplets, or they are considered activated if the largest radius is given at the final time-step. To get the time of activation for each activated droplet, we find the inflection point of the radius over time (thus this method can only be applied in post-processing) by calculating a proxy for the second-derivative of the radius, taking the logarithm of the absolute value, and finding the maximum:

$$r_c = \max \left(\log_{10} \left| \frac{d^2 r}{dt^2} \right| \right).$$

2.1.5 Numerical Details

The entirety of the model is coded in Python and utilizes the numba package (Lam et al., 2015) to markedly speed up computational time and efficiency. The mass growth rate equation for condensed water (3) is solved using a Runge-Kutta Cash-Karp method. This allows for error estimation and subsequent adaptive time-stepping by calculating both 4th and 5th order solutions, with the difference between them being used for the adaptive time-step adjustment. The new time-step size is then used for all other time-dependent equations, which are solved using a simple Forward-Euler scheme (co-condensation, environmental variables, and particle motion). Stability is not an issue in this case for these equations due to the small time-step size derived from the water-mass growth equation. For further documentation on the coding details, readers are referred to an accompanying github directory and the instruction manual there¹.

2.2 Internal Error Estimation From Variability

While one of the main advantages of this model is its simplicity and low computational requirements (such that it can be run on any current laptops or personal computers), it is still limited in the size of its domain and the number of particles it can contain due to eventual memory limitations and poor scaling in terms of computational cost (a 10 cm³ volume can easily ap-

¹<https://github.com/dBarthaux/PARCELY>

proach 1 hour of run time for 200 seconds of model time). When simulating non-monotonic aerosol distributions, the small sampling size leads to potentially large variability in solutions for environmental variables or the activated fraction of the droplets. This is an issue similar to the one faced by meteorological and climate models, where the internal variability can lead to different results due to uncertainties in initial conditions (Lucas-Picher et al., 2008). Such models can perform runs with slightly varying initial conditions to look at a range of possible outcomes from the different runs. These are called “ensemble forecasts” and each run is a “member.” A larger number of members can increase the confidence in a forecast, or at least aid in quantifying the uncertainty (Milinski et al., 2020).

In the PARCELY model, the internal variability stems from the random sampling from a non-monotonic distribution. Because the model is limited to a total particle count on the orders of up to 10^3 , any sampling will not be able to fully capture the nature of the entire distribution, as seen in Figure 4.

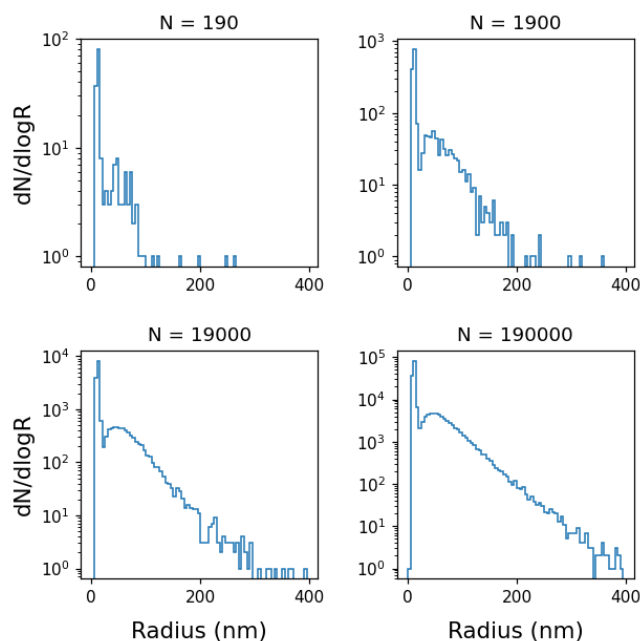


Figure 4: Example of how total simulated particle count changes the shape of the sample distribution. Size distributions (radius, nanometers) of the dry particles (dry seed aerosols) in log-scale are sampled from the same bimodal-lognormal aerosol distribution of typical “pristine conditions”. Here, N is the total number of particles.

To address the internal variability, the model should be run with the same initial conditions but different random number generator seeds. This is essentially the same technique as described for climate models, but here the only variation occurs in the sample from the aerosol size (radius) distribution; no other initial condition is altered. While one can choose to have as many members in their run as they wish, having the smallest number of members while still capturing the internal variability to an acceptable degree is the optimal path forward.

Table 1: Parameters for the four aerosol population distributions used throughout the thesis. Mean radius and standard deviation are geometric unless marked with a star indicating arithmetic.

Name	Distribution	Number Concentration (cm^{-3})	Mean Radius (μm)	Standard Deviation (μm)
Mono	Monodisperse	190	0.05*	-
Normal	Normal	190	0.05*	0.01*
Pristine	Bi-modal log-normal	190	0.011 (N=125), 0.060 (N=65)	1.2, 1.7
Polluted	Bi-modal log-normal	540	0.029 (N=160), 0.071 (N=380)	1.36, 1.57

Three tests were performed to estimate the generally optimal number of members. In each test, 150 members with a 1 cm^3 parcel volume, and 10 members with a 10 cm^3 parcel volume were run, each one with a unique generator seed. The mean of the 10 large-domain members (and 10-times larger amount of particles) was taken to be the representative “true” solution for both environmental saturation ratio and activated droplet fraction. The three test cases for the aerosol size distribution were a normal, pristine, and polluted distribution (details in Table 1, (Andrejczuk et al., 2008, Grabowski et al., 2011)). The seed aerosol used was ammonium sulfate, with a κ value of 0.61.

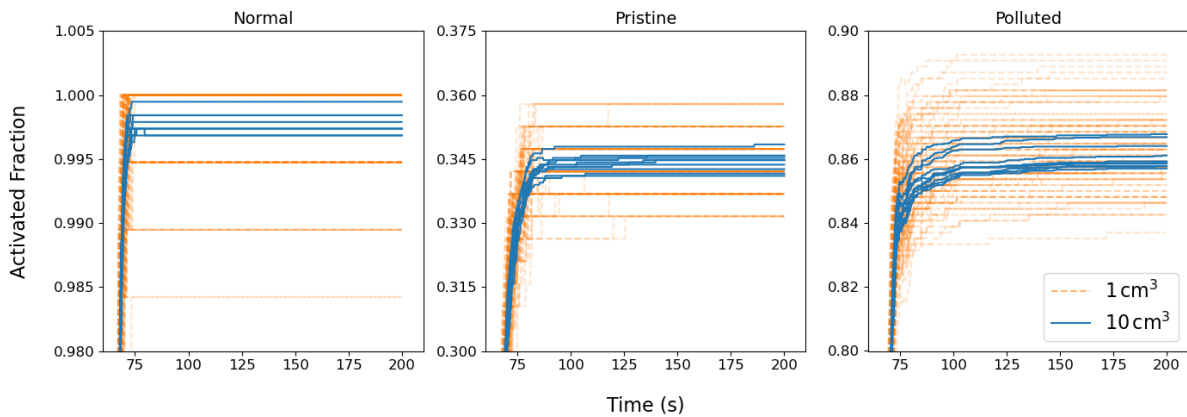


Figure 5: Activated fraction (the number of activated CCN over total number of CCN) for the three test aerosol size distributions in Table 1 using 150 of the 1 cm^3 (orange) and ten 10 cm^3 (blue) parcels. The orange lines are made to be more transparent to better show overlapping of results (darker shades). The y-axis scales differ for each plot.

Figure 5 shows the activated fractions for the small and large parcels. There is a noticeable grouping of solutions for the small parcels in Normal and Pristine distributions, and the large parcels in the Polluted distribution. This “bunching” is also seen in the solutions for the environmental saturation ratios (not shown). This feature is a result of the smaller sampling – it is shown for the log-normal cases that the mean activated fraction of the small volumes (orange)

is indicated by the larger volumes (blue). For the Polluted case, the number concentration is still large enough that the solution has not converged yet, but the range of values has been significantly narrowed. It is important to note that the variation in the number of activated droplets for the smaller parcels is limited to 4 (Normal), 5 (Pristine) and roughly 40 (Polluted). This leads to an illusion of larger deviations when looking at activated fractions, while in reality the activated particle count could differ only by one or two particles, depending on the distribution.

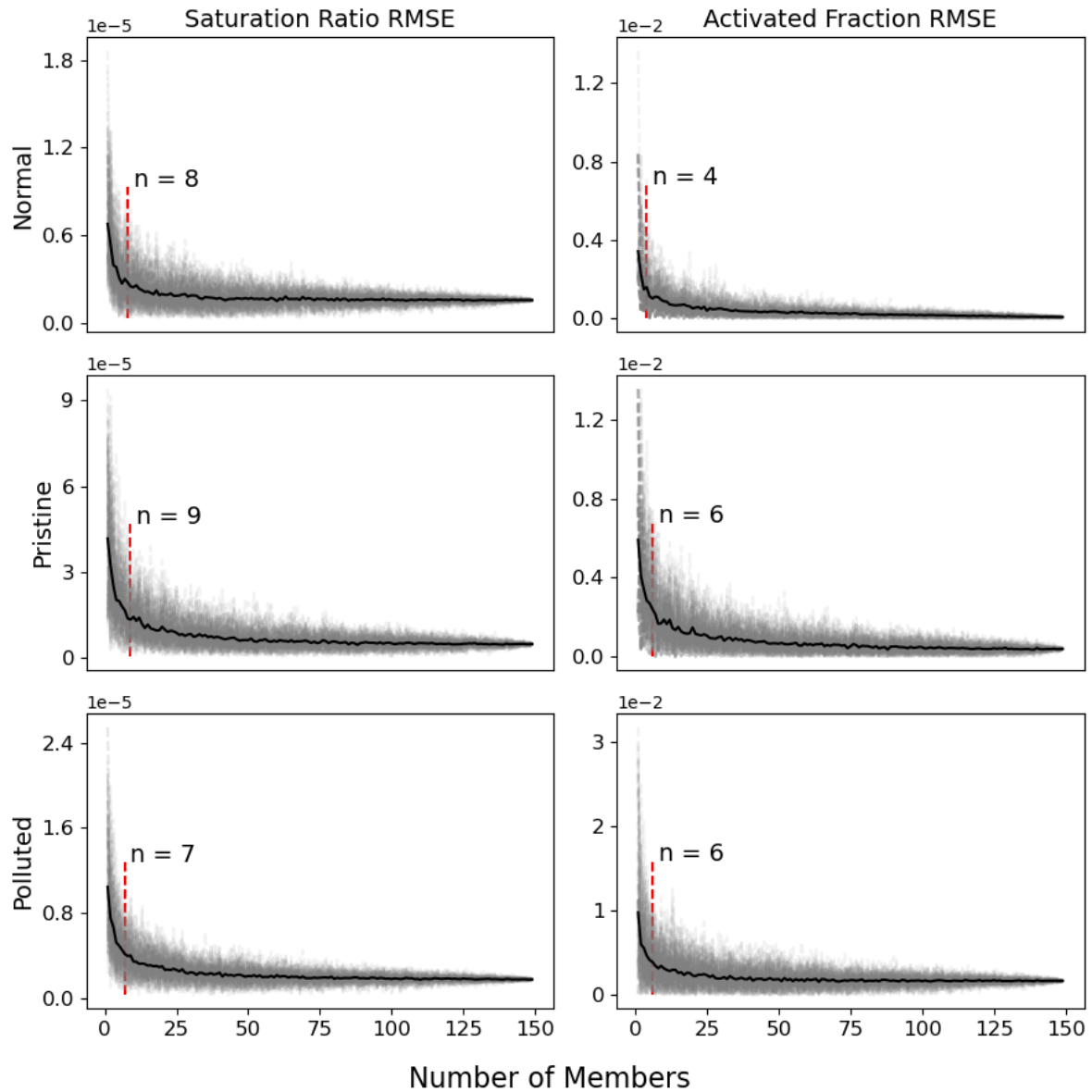


Figure 6: Root-Mean-Square-Error (RMSE) of saturation ratio and activated droplet fraction (Activated CCN/Total CCN) of 1 cm^3 parcel runs for three test distributions (Table 1), one per row, as a function of number of members used. The “true solution” is taken to be an average of ten 10 cm^3 runs. The mean is shown in solid black, and the e-folding member number (37 % of the initial mean value) of the mean is marked by the red dashed line.

Figure 6 shows the root-mean-square errors (RMSE) of each distribution for saturation ratio and final time-step activated fraction with increasing number of members. The members are chosen at random and without replacement from the 150 simulations, and this is done 100 times

Table 2: Input for the aerosol population and environmental initial conditions to recreate the data from Chen et al., 2020 in the PARCELY model.

Variable/Parameter	Values
Particle Concentration (cm^{-3})	100
Distribution Type	Monodisperse, ammonium sulfate
Solute Radius (μm)	0.1
Saturation Ratio (%)	85.61
Temperature (K)	284.3
Pressure (Pa)	93850
Updraft (m s^{-1})	2

(gray lines in the figure), creating 100 RMSE profiles. For the activated fraction, the polluted case has the highest RMSE ($\approx 3 \times 10^{-2}$), while the highest RMSE for saturation ratio is in the Pristine distribution ($\approx 10 \times 10^{-5}$), both occurring for either only 1 or 2 members. The former is expected and touched upon previously, while the latter suggests that the saturation ratio becomes much more sensitive to sampling variations when the number concentration decreases. After repeated testing, every error's e-folding member (defined here as reaching 37 % of the initial mean value) amount was found to mostly oscillate around 10 members. This suggests that using a volume of 10 cm^3 or 10 separate model runs would result in adequate statistical representation of a model using much larger volumes and number of simulated particles.

2.3 Validation

To validate the model, test cases from Thomas et al. (in preparation) and Chen et al., 2020 were used for output comparisons. Thomas et al. use a pure DNS model to simulate the air parcel and solve for individual droplets as well as for the turbulent water vapour field and air motion within the parcel, while Chen et al., 2020 use a hybrid parcel–DNS model. Differences in parameter values, as well as slight alterations in environmental constants (such as the latent heat of condensation, mass and thermal accommodation coefficients, or the specific gas constant for water vapour) had to be accounted for in order to accurately perform the comparison tests. For more detail regarding the compared models, the reader is referred to their respective papers.

Excellent agreement was found for all initial aerosol size distributions compared against the results from Thomas et al. in both growth and activation of the droplets in the pristine and polluted populations, as well as mean environmental values. Unfortunately, data from the original publications to plot the comparisons could not be attained for Thomas et al.'s comparisons. Figure 7 compares PARCELY's supersaturation and mean droplet radius with the DNS model by Chen et al., 2020 for an initially mono-disperse aerosol population with Table 2 listing the input variables used. Some differences are noticeable in both profiles, noticeably the peak in supersaturation and the time of activation. However, they are qualitatively similar enough to

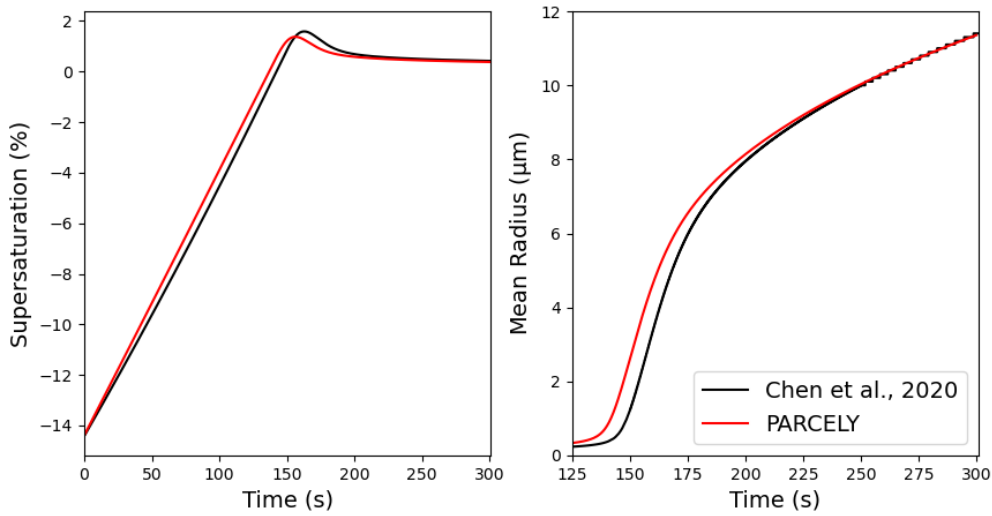


Figure 7: Comparison of supersaturation (left) and mean wet radius (right, arithmetic, all droplets) evolution over time between the parcel model used in Chen et al., 2020 (black) and the PARCELY model (red). Note that the radius plot starts at 125 seconds in order to avoid the extremely large oscillations in Chen et al.’s data. The mass and thermal accommodation coefficients in PARCELY were assumed to be the values from Pruppacher et al., 1998.

establish a case for model validity. In addition, the cause of the discrepancy might be purely due to noise in the initialization of their simulation; their data for the mean wet radius only stabilizes after 125 seconds, with oscillations spanning several orders of magnitude before that point. If the time-step is too large, PARCELY will return similar results and this can lead to shifts in both the peak supersaturation and the time of activation.

To compare our organic-film method with a reference simulation, we use the results from Lowe et al., 2019. We adopted their prescribed input variables and parameters listed in their Table 1 and Figure 1b. Their model does not use κ -Köhler theory, so for the organic hygroscopicities we use 10^{-5} for pinic acid (Petters and Kreidenweis, 2007) and 0.025 (estimated using the AIOMFAC model) for the surrogate systems. Additionally, they do not use an adjusted thermal conductivity equation, only an adjusted water vapour diffusivity equation with an accommodation coefficient of unity. We set both accommodation coefficients equal to unity in the PARCELY model for the purpose of this comparison.

Figure 8 shows the evolution of supersaturation and droplet number concentration (or activation count) as simulated by the PARCELY model in comparison to the spectral-bin model used by Lowe et al., 2019 for runs with a compressed organic film approach and without (“bulk Köhler”). All of PARCELY’s predictions lie closer to the film approach or equally distant from it and the bulk approach, which is favorable. The model deviations increased with increased particle concentration (360, 1650, 2030 for Marine, Boreal, and NUM respectively). This could be due to the sampling issue and internal variability discussed in section 1.2, however after testing the Marine case with a larger domain size, no substantial improvement was

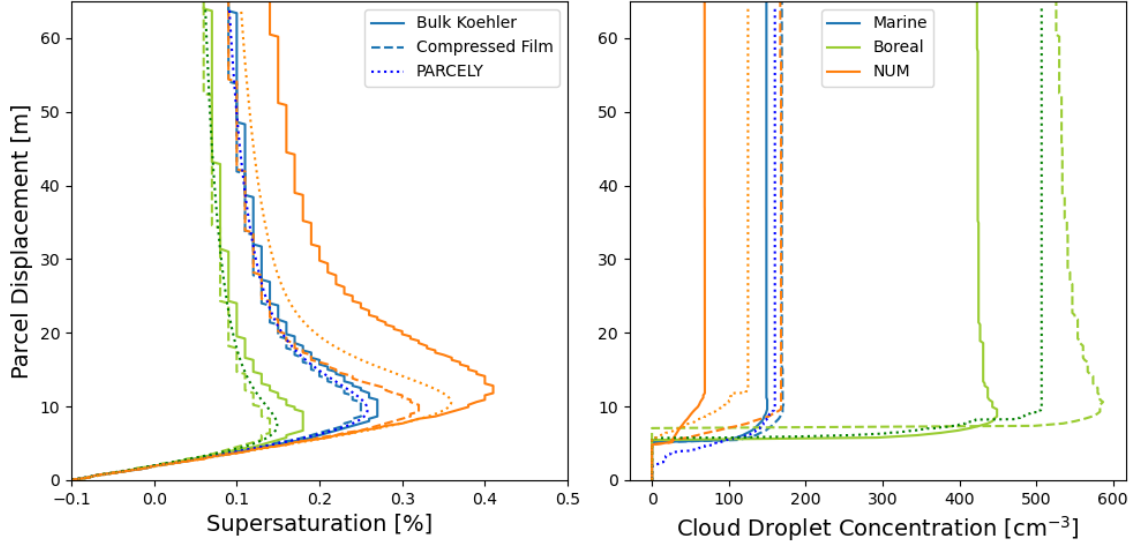


Figure 8: Comparison of supersaturation (left) and droplet concentration (right) evolution with height between the PARCELY model and the spectral-bin model used in Lowe et al., 2019, recreating their Figure 2 (a,b). Solid lines mark their model’s bulk-Köhler approach, dashed lines denote their model’s compressed organic-film method, and the dotted lines show predictions when using PARCELY’s organic-film method. Marine and Boreal are representative aerosol size distributions of their environments, with the former being mostly inorganic in composition and the latter mostly organic. NUM represents a nascent ultrafine mode event distribution with roughly equal solute composition.

noticed. It is possible then that the discrepancies are caused by differences in thermodynamic parameterization or defined constants. Overall though, the comparison satisfies the validation of PARCELY’s capabilities and suggest that the model’s various features are free of major flaws in their implementation.

Co-condensation was validated against basic test cases from Topping, 2022 and the kinetic multi-layer model for gas-particle interactions model (KM-GAP) from Shiraiwa et al., 2012 to confirm that no errors in coding or numerics are present. PARCELY successfully reproduced output from both models, confirming the validity of our co-condensation equations.

3 Sensitivity Analyses

3.1 Impact of Accommodation Coefficients

3.1.1 Motivation

Even when looking only at parcel sizes on the order of 1 cm^3 , parameterizations are still needed in several equations of a parcel model. One of these key parameterizations addresses the fact that the equation used for condensational growth assumes that the fields of the environmental variables (heat, water vapour, pressure) are approximated as continua (rather than resolving the positions, velocities and elemental makeup of each molecule in air). This approximation is justifiable when the Knudsen Number, the ratio between the mean free path in air and the radius of the droplet, is much smaller than one, which holds for large drops. In the inverse scenario, equations from molecular collision theory can be used (Seinfeld and Pandis, 2016). In the initial stages of growth however, the Knudsen number can reside in neither regime. In such a case, one can describe the growth occurring as if in a continuum while still experiencing the kinetic effects from the molecular collision theory. These kinetic effects are represented via their impact on the diffusivity of water vapour and the conductivity of heat in air. There have been several equations developed over time to describe this treatment, each with slightly differing forms or sets of parameters (Fukuta and Walter, 1970, Carstens et al., 1973, Rossow, 1978).

In this experiment with the PARCELY model, we aim to look at the impact of the mass accommodation coefficient α_c (also known as water uptake coefficient) and the thermal accommodation coefficient α_T present in the adjusted expressions for diffusivity and thermal conductivity, respectively (see section 2.1.2). The former represents the fraction of water molecules impinging on the surface of a droplet that are taken up by the droplet, and the latter is the fraction of colliding molecules that achieve thermal equilibrium with the droplet's surface. The accommodation coefficients are considered to be a significant source of uncertainty in process-level cloud models due to their indirect effect on the peak supersaturation attained at cloud base, and therefore the activated number of droplets one can then attain (Raatikainen et al., 2013). Determining their range of values with accuracy thus could have long-reaching impacts on climate and weather prediction models that use them directly in their parameterizations for cloud droplet concentrations, or indirectly from parameterizations reliant on parcel models that use them.

There have been many different attempts to constrain the water uptake coefficient through laboratory work (Li et al., 2001, P. M. Winkler et al., 2004), field experiments (Fountoukis et al., 2007), and numerical models (Vesala et al., 1997). Recent research has posited that it lies between 0.1 and unity (Davidovits et al., 2004, Miles et al., 2012), while earlier work had the

range an order of magnitude lower (0.01 and 0.1; Shaw and Lamb, 1999, Zagaynov et al., 2000). Issues arise mainly from the fact that these coefficients are not directly measurable, and different techniques or approaches lead to differing definitions and interpretations, and obtained values.

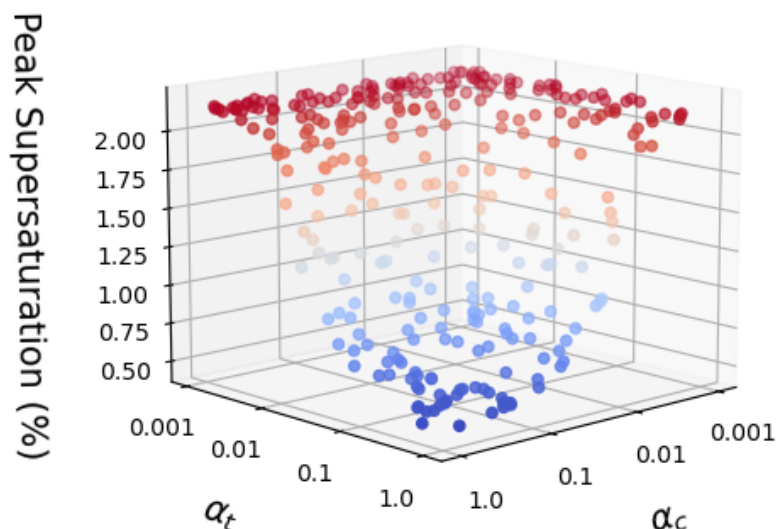


Figure 9: Peak supersaturations of 300 model runs with varying mass (α_c) and thermal (α_t) accommodation coefficients. All simulations used a mono-disperse distribution (190 cm^{-3}) of 50 nm dry-radius particles of ammonium sulfate and an updraft velocity of 1 m s^{-1} and were run for 200 seconds. The peak supersaturation is also represented by the colouring of the points for additional clarity.

The reduction of the α_c range to 0.1–1 is already substantial as demonstrated in Figure 9, which shows a dramatic change in peak supersaturation when values for α_c or α_t are allowed to vary by several orders of magnitude below 0.1, while keeping all other parameters constant. The peak supersaturation reached near cloud base levels off towards coefficients values on the order of 10^{-3} . This is both physically and mathematically expected. As the coefficient decreases in size their respective parameter (diffusivity of water vapour or thermal conductivity) converges to zero (see Eq. (12) and (13)). This acts to enlarge the denominator in the growth rate equation (3), thus reducing the condensational growth rate. Physically, for the mass accommodation coefficient this means fewer water molecules hitting the droplet are condensing or absorbed into it, and so stay in the ambient air. For the thermal accommodation coefficient, fewer water molecules equilibrate with the droplet and thus have a higher chance of quasi-instantaneous desorption from the droplet surface back to the free gas phase (“escaping”).

On a larger scale, Raatikainen et al., 2013 showed through analysis of multiple global data

sources that a mass accommodation coefficient of 0.2 is able to capture the temporal variability of droplet radii in climate models with a constant bias. At the molecular level, Barclay and Lukes, 2019 found through molecular dynamics simulations that mass accommodation coefficients have a size-dependence, with the value converging to α_∞ , the coefficient for an infinitely-large or zero-curvature particle surface. We argue that this size-dependence can be neglected for most cloud parcel models, as the convergence to a singular value for water starts to dominate at radii beyond 2 nm (at typical atmospheric temperatures). Their predicted α_∞ range from 0.1–0.28, though for temperatures beyond 500 K.

Research into determining the true value of the thermal accommodation coefficient has been much sparser compared to research into its mass counterpart. Its value has similarly been limited to the range of 0.1–1 (Shaw and Lamb, 1999, Sageev et al., 1986), although values closer to unity have been more commonly cited (Alty and Mackay, 1935, Li et al., 2001, Viececi et al., 2004). Purely by looking at the contributions of the conductivity and diffusivity terms to the growth equation, there is no reason to think that the thermal accommodation coefficient should be any less important, considering that both coefficients have been determined to vary within the same range of values.

3.1.2 Results

Despite this narrowed range for both coefficients, even allowing them to vary in value between 0.1 and unity can have a discernible impact on the peak supersaturation attained during parcel ascent and droplet activation. Figure 10 shows the effects of the variation in this range on the the peak supersaturation of the distributions detailed in Table 1. The highest values of supersaturation continue to occur when the coefficients are smallest.

Additionally, the thermal accommodation coefficient is the dominant of the two, as can be seen from the tighter clustering of values along the descending slope. The mass accommodation bears the same profile, but the varying values of α_T lead to more scattering. This difference is made even clearer when normalizing the data, as seen in Figure 11. The supersaturation profiles all collapse onto the same slope, which is more visibly detectable for the thermal accommodation coefficient variation than for the mass accommodation coefficient variation. The normalization follows the min-max feature scaling:

$$s' = \frac{s - \max(s)}{\max(s) - \min(s)} \quad (27)$$

When looking at the number of activated droplets in Figure 12, the effect of varying the coefficients vanishes for both the monodisperse and normal distributions; the former having all droplets activate regardless of supersaturation variation, and the latter having only slight deviations from total activation due to internal variability (see section 2.2). The result would likely

vary substantially if a different dry size or updraft velocity were used. One could possibly find a combination where the change in accommodation coefficients could make a meaningful impact on the number of activated droplets. The influence of the accommodation coefficients does appear however through the mean droplet radius (not shown). As the coefficients approach unity, the mean radius for the mono-disperse gradually increases to a maximum value. For the rest of the distribution cases, the results for the dependence of the mean droplet radius mimic those for the number of activated droplets. The range of values in the mean radius when varying the accommodation coefficients is limited: 0.006, 0.06, 0.2, and 0.4 μm for the mono-disperse, normal, pristine, and polluted distributions respectively.

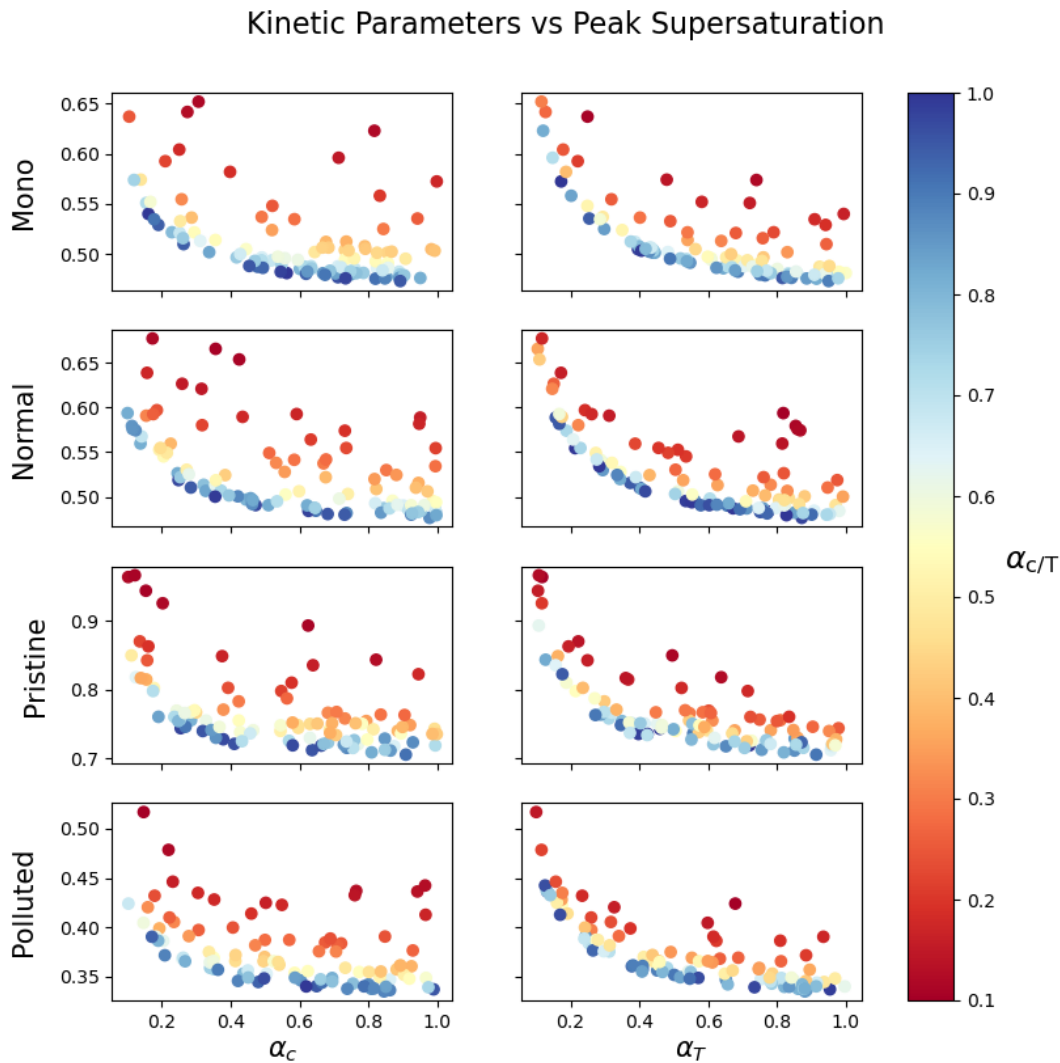


Figure 10: Peak supersaturation (in percentage) variation with changing mass and thermal accommodation coefficients ranging from 0.1 to 1. Each distribution was sampled in 100 independent model runs (using uniformly sampled accommodation coefficients from the state range) with a 1 m s^{-1} updraft velocity and run-time of 200 seconds. The only variations between runs are the coefficients and the random seed generator, which leads to internal variability in initial dry sizes. The particle concentrations are 190 cm^{-3} except for the polluted case (final row) which has a particle concentration of 540 cm^{-3} . The color bar on the right shows the value of the other accommodation coefficient.

In the pristine distribution we only see a possible influence of coefficient values when they are

both small, as indicated by the upper left hand corners of the pristine plots. However, the total range of values does not exceed the range attained from internal variability (± 5 droplets), implying that the coefficients have no discernible impact. The rest of the data points are scattered homogeneously around 65 activated droplets regardless of either coefficient's value. It is only in the polluted distribution where we see a clear connection, where the range of values possible from internal variability is exceeded. A similar negative trend with increasing coefficients as in 10 can be seen - however only for the thermal accommodation coefficient. This once again strengthens the case for it being the dominant of the pair.

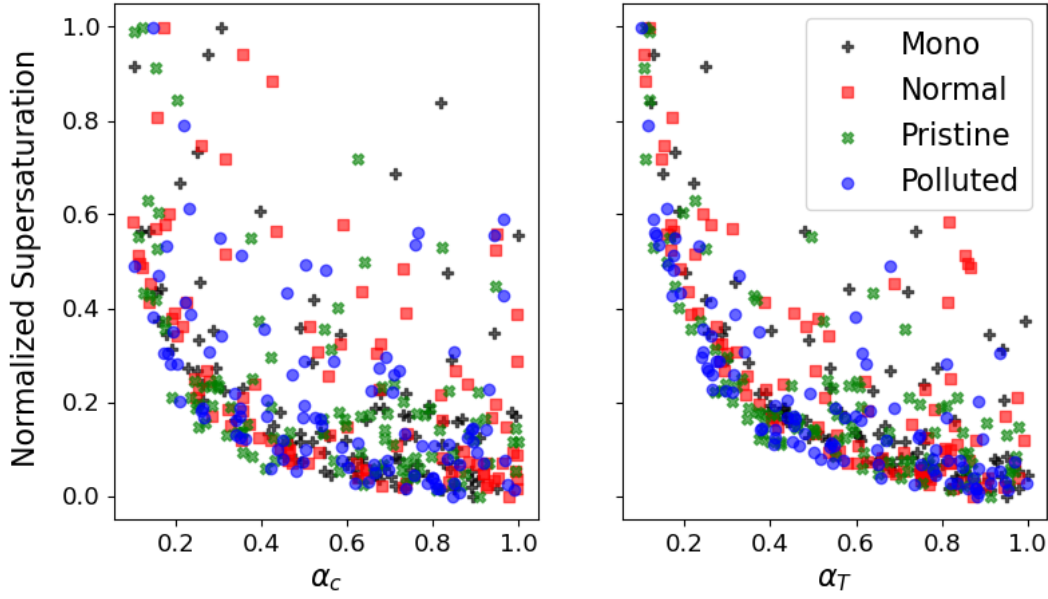


Figure 11: Data from Figure 10 normalized using min-max feature scaling shown in Eq. (27).

To gain more insight on the influence of size distribution and number concentration, we arbitrarily doubled (halved) the number concentration of the pristine (polluted) distribution. The halved polluted case showed much weaker/less correlation between the number of activated droplets and the accommodation coefficients, and the doubled pristine distribution returned similar results to its original version. Despite this, the supersaturation dependence for both altered distributions were qualitatively identical to their original versions. This shows that the relation between activated droplets and accommodation coefficients is not as straightforward as the latter with supersaturation, and heavily depends on the number concentration and size distribution of the aerosol population present. It can be concluded that for more polluted conditions (CCN number concentrations greater than 400 cm^{-3}), the influence of the parameter choices becomes notable, since it is less likely under those polluted conditions that all CCN will activate at reasonable updraft speeds.

When using the same predefined values for the accommodation coefficients for all four distributions, the standard deviation of the normalized peak supersaturations between different

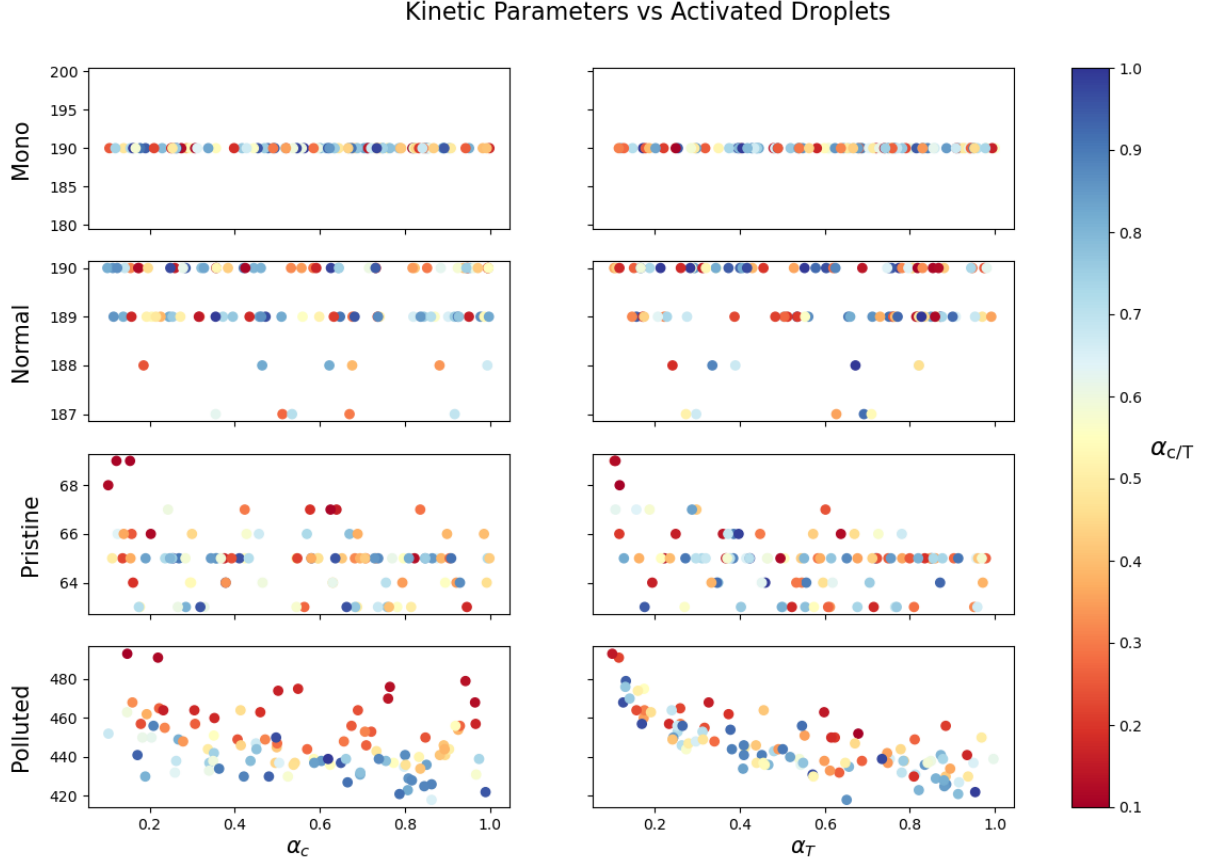


Figure 12: Activated droplet count variation with changing mass and thermal accommodation coefficients ranging from 0.1 to 1. Each size distribution was adopted for 100 model runs in total with a 1 m s^{-1} updraft velocity and run-time of 200 seconds. The only variations between runs are the coefficients and the random seed generator, which leads to internal variability in initial dry sizes (each run has random values for the two accommodation coefficients). The color bar on the right shows the value of the other accommodation coefficient. The particle concentrations are 190 cm^{-3} except for the polluted case (final row) which has a particle concentration of 540 cm^{-3} .

distributions had a maximum of only 0.0051 (supersaturation), suggesting that the effect of altering the accommodation coefficients on the normalized data is identical regardless of size distribution used. A polynomial expression with monotonically increasing values for both coefficients as variables was fit to the mono-distribution normalized data using MATLAB's Curve Fitting toolbox (The MathWorks, 2020):

$$s_{\text{peak,normalized}} = 1.148 - 1.166 \alpha_c - 1.872 \alpha_T + 0.7869 \alpha_c^2 + 0.06546 \alpha_c \alpha_T + 1.242 \alpha_T^2 \quad (28)$$

One could possibly utilize this expression to calibrate their models or tune their instrumentation if their assumed value for a coefficient does not match an observed peak supersaturation. This would likely require solving an inverse problem based on Eq. (28), where one is given a normalized supersaturation and would need to determine the accommodation coefficients from it.

A Monte-Carlo simulation was performed to determine the impact of the uncertainty in the

range of values for the accommodation coefficients when compared to varying the dry particle radius and updraft velocity. 352 model runs with a mono-disperse distribution of ammonium sulfate aerosols were completed. The accommodation coefficients, dry particle radius, and updraft velocity were randomly selected from a uniform distribution in the ranges of 0.1–1, 10–100 nm, and $0.5\text{--}5\text{ m s}^{-1}$, respectively. All other initial conditions were identical. The results are shown in Figure 13, and data from a multiple linear regression analysis is listed in Table 3.

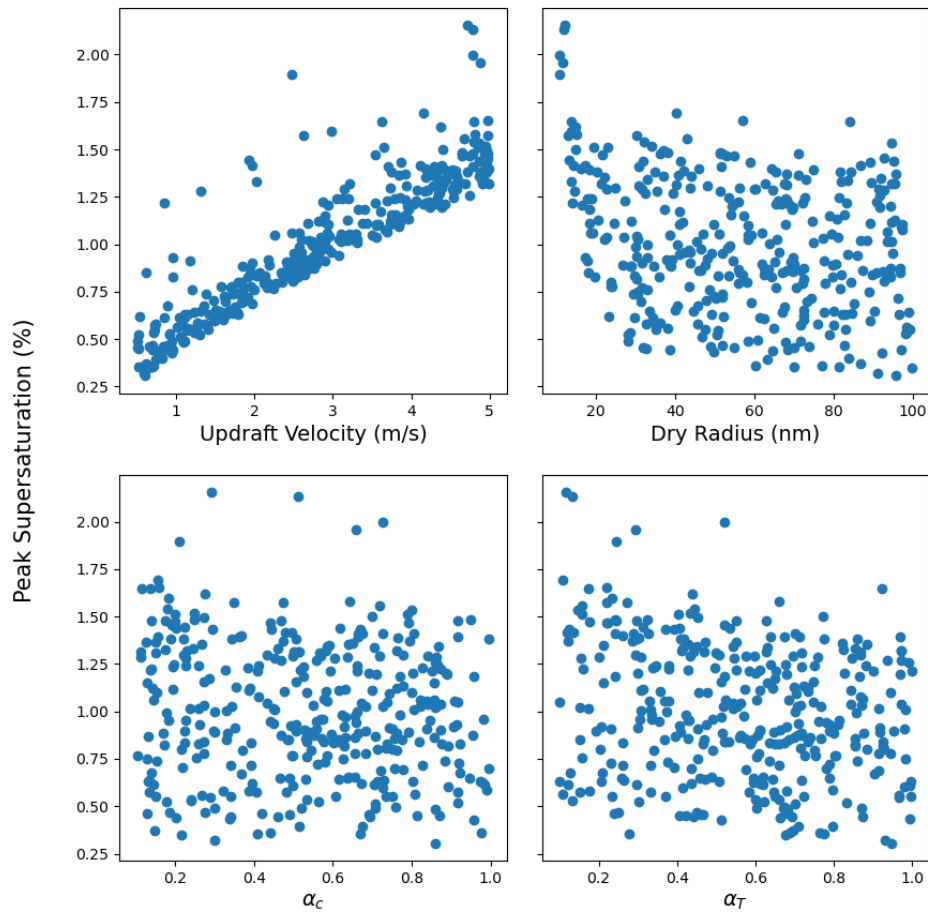


Figure 13: Results of a Monte-Carlo simulation experiment to capture the change in peak supersaturation with varying updraft velocity, dry radius, and mass and thermal accommodation coefficients. Here 352 simulations each with a 200 second run-time were performed.

It is evident from both the figure and the statistics that the updraft velocity is the governing variable and is quite clearly linearly related to the peak supersaturation. This is obvious from its mathematical relation (see Eq. (6)). The dry radius is weakly correlated with a smaller t-score, however this result does not imply that the correlation is indeed weak, but rather that the relation is not a simple linear one. From Figure 13 we can at least conclude that the smallest dry radii are associated with the largest peak supersaturations and vice-versa. This can be more clearly seen in Figure 14; smaller radii will lead to higher peak supersaturations than larger ones for the same updraft velocity. No visual connection between supersaturation and either accommodation coefficients can be readily seen, although the statistics bolster the claim that

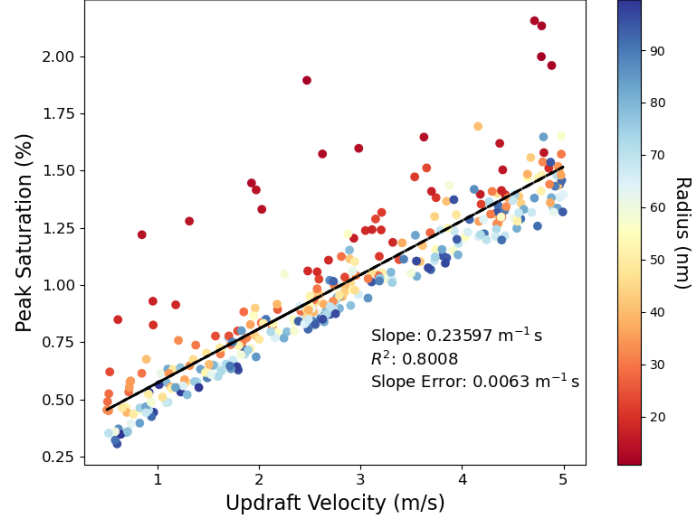


Figure 14: Enlargement of the updraft velocity versus peak supersaturation from Figure 13, with the color scheme representing the dry radius. The results of a linear regression model are shown by the black dashed line.

Table 3: Results from the multiple linear regression performed on the Monte Carlo test for a mono-disperse aerosol size distribution targeting peak supersaturation.

	Correlation	Coefficient	Standard Error	t-score
Updraft	0.89	0.2332	0.004	56.063
Dry Radius	-0.28	-0.0036	0.0	-16.323
Mass	-0.12	-0.1756	0.025	-7.917
Accommodation				
Thermal	-0.23	-0.2274	0.023	-10.017
Accommodation				
Constant	-	0.7679	0.025	31.155

the thermal coefficient is more dominant than its mass counterpart. These results once again assume a linear relationship, whereas it has been shown that the relation is best approximated as a polynomial.

Our last experiment is to repeat the same Monte-Carlo test, but using the pristine and polluted distributions detailed in Table 1, which are more realistic representations of CCN distributions one would find in the atmosphere. 200 simulations with different seeded generators for both of the distributions were run, with varying updraft velocity, accommodation coefficients, mean dry particle radii, and standard deviation for the radii. This gives seven variables (two modes in the distribution, so two mean radii and two standard deviations) for the multi-linear regression. We looked at the variation in the number of activated droplets as well as the peak supersaturation. As with the mono-disperse test, the variables were randomly selected from uniform distributions. The range of mean radii values were $\pm 0.03 \mu\text{m}$ around their original values, and the standard deviations $\pm 0.1 \mu\text{m}$ around their original values (see Table 1). The range of the accommodation coefficients values was identical to the mono-disperse test, while the updraft

Table 4: Results from the multiple linear regression performed on the Monte Carlo test for the Polluted bimodal log-normal aerosol size distribution targeting peak supersaturation and number of activated droplets. Numbers in red indicate results that do not pass the significance test ($\alpha < 0.05$).

Variable	Supersaturation Correlation Coefficient	Supersaturation t-score	Activation Correlation Coefficient	Activation t-score
Radius 1	0.052	-2.165	0.27	7.364
Radius 2	-0.15	-3.999	-0.072	0.227
Radius Standard Deviation 1	0.011	0.075	0.066	0.371
Radius Standard Deviation 2	-0.0091	-1.752	-0.1	-4.717
Mass accommodation coefficient	-0.16	-11.447	-0.1	-6.276
Thermal accommodation coefficient	-0.27	-16.244	-0.21	-9.345
Updraft velocity	0.91	52.301	0.89	36.234

velocity was allowed to range from 0.1 m s^{-1} to 1.5 m s^{-1} .

The correlation coefficients and t-scores from the Monte-Carlo experiment on the bimodal distributions (pristine, polluted) are shown in Tables 4 and 5, ignoring the added constant. Initial analysis of the Monte-Carlo results showed no obvious visual relationship between any of the variables and peak supersaturation or droplet activation apart from updraft velocity. In addition, 22 (24) runs were removed from the 200 pristine (polluted) simulations due to the model being run for an insufficiently long enough time given updraft velocities below 0.3 m s^{-1} .

Looking at the polluted case, the updraft velocity is the dominant factor for determining both the peak supersaturation and the number of activated droplets. As expected, the accommodation coefficients have negative correlations and t-scores (higher values mean more water uptake, which both lowers the peak supersaturation and decreases the amount of water vapour unactivated droplets can use to grow via condensation). They are more correlated to the peak supersaturation than the number of activated droplets however, with the smaller mean radius becoming more important for the latter. The standard deviations are either not statistically significant, or are inconsequential when considering the two variables in question.

The pristine case is qualitatively identical, except for the sign of Radius 1 for the supersaturation correlation. Given that the t-score was determined to be statistically insignificant, and that the correlation coefficient is quite small (-0.0092), we do not make any conclusions from this. We

Table 5: Results from the multiple linear regression performed on the Monte Carlo test for the Pristine bimodal log-normal aerosol size distribution targeting peak supersaturation and number of activated droplets. Numbers in red indicate results that do not pass the significance test ($\alpha < 0.05$).

Variable	Supersaturation Correlation Coefficient	Supersaturation t-score	Activation Correlation Coefficient	Activation t-score
Radius 1	-0.0092	-0.649	0.38	7.482
Radius 2	-0.1	-2.139	-0.088	0.363
Radius Standard Deviation 1	0.048	-0.453	0.3	4.973
Radius Standard Deviation 2	-0.013	0.194	-0.032	-0.338
Mass accommodation coefficient	-0.075	-9.281	-0.16	-2.830
Thermal accommodation coefficient	-0.16	-14.782	-0.17	-3.112
Updraft velocity	0.96	80.033	0.55	11.223

see that the accommodation coefficients have generally smaller correlation coefficients and t-scores for the pristine case than the polluted, likely due to the larger number concentration of CCN in the latter distribution, and the larger impact it has on the environmental supersaturation. Additionally, the standard deviation for Radius 1 has a noticeably higher correlation coefficient and t-score for droplet activation in the pristine case (0.3 compared to 0.066), due to the shape of the aerosol size distribution. Since most of the CCN from this aerosol mode do not activate, a larger standard deviation for the mode will directly contribute to the number of activated droplets by initializing more CCN with bigger dry particle radii.

3.1.3 Discussion

In an ideal scenario, the value for the mass and thermal accommodation coefficients would be calculated as a function of easily attainable variables in cloud parcel models, such as temperature, saturation ratio, or particle composition. While we have seen that perhaps such a function may not be necessary for atmospherically relevant models and that adopting a constant value may be adequate, the lack of any consistent and agreed-upon values for each of the coefficients warrants a cautious and deliberate choice when selecting values from reported measurements or modelling.

Here, we quantified the effects of varying either coefficient in the range of 0.1–1, informed by recent research in modelling and laboratory experiments. We showed that despite the focus on

the mass accommodation coefficient, it is in fact the thermal coefficient that is slightly more important in affecting supersaturation levels, and thus the number concentration of activated particles. In addition, we showed that the profile of the variation in peak supersaturation (attained near cloud base) is not sensitive to the distribution used, with only the range of values changing (the shape is the same). Proper scaling centers all values to a single approximate profile, fitted to a polynomial equation. The determined equation (Eq. (28)) could potentially be used to adjust coefficients to fit a measured value of supersaturation, or possibly calibrate an instrument reliant on them.

Finally, we performed a Monte Carlo test on a mono-distribution, pristine-, and polluted-bimodal distribution of particles with varying updraft velocity, mean dry radius, dry radius standard deviation, and kinetic coefficients. Using multiple linear regression, it was shown that the updraft velocity is the dominant determining factor for the peak supersaturation, and to a lesser extent the number of activated droplets. The thermal accommodation coefficient had consistently larger or roughly equal correlation coefficients compared to the mass accommodation coefficient, suggesting the need to focus research efforts into it alongside research into the mass coefficient. When the updraft velocity is unknown, the values chosen for the coefficients can be considered less crucial (when using the 0.1–1 range for the accommodation coefficients), freeing researchers to look at the effects of other variables without worrying about their choice of kinetic correction parameters.

3.2 Heterogeneous Ambient Fields

3.2.1 Motivation

While parcel models often use a single value for the saturation ratio - and hence supersaturation - throughout their domain, the reality is that clouds experience turbulent variations in temperature and water vapour mixing ratio that lead to variations in supersaturation (Shaw, 2003). From a recent study of cumulus formation, spatial and temporal fluctuations of 1 % in saturation ratio were measured at cloud base (Siebert and Shaw, 2017) which would affect droplets differently depending on which levels of supersaturation they are exposed to. Turbulence is considered to be a key mechanism in broadening the droplet size distribution to allow for the onset of collision-coalescence and subsequent precipitation formation (Grabowski and Abade, 2017).

As with most issues plaguing the accurate representation of clouds in weather and climate models, the turbulence that affects the microphysics of clouds is much too small to ever be simulated within these models in the foreseeable future. The turbulent eddies in question can be categorized by characteristic length scale into dissipative (1 mm–1 cm), inertial-range (10 cm–10 m), and entraining (100 m) eddies (Grabowski and Wang, 2013). High-resolution weather models have grid sizes of at least several kilometers (Wedi et al., 2020), limiting them to turbulent features on the cloud scale. Large Eddy Simulations (LES) have been developed to simulate the turbulent features in the entraining and partially in the inertial range (e.g. Khairoutdinov and Kogan, 1999, Feingold et al., 1994); however, even their grid resolutions are too large to resolve the eddies in the dissipative scale.

To simulate the smaller inertial-range and dissipative range eddies, the use of Direct Numerical Simulation (DNS), or high-resolution LES models is required (e.g. Thomas et al., 2019). These models have been used successfully to resolve the important small-scale turbulence impacting the microphysics within a cloud environment (e.g. Kumar et al., 2018, Codoni, 2018, MacMillan et al., 2022), but performing such simulations comes at great computational cost. High-performance, massively parallelized supercomputers are needed and the run time can be considerable. This limits the number of runs one can perform with different inputs when compared to the ease of use of simpler cloud parcel models like PARCELY, although a parcel model captures much fewer aspects of cloud microphysics and, unlike LES models and research-level mesoscale weather models, parcel models do not capture the cloud-scale evolution and dynamic interactions with the broader cloud environment.

With this in mind, the aim for this experiment here is to introduce a gridded field of saturation ratio and temperature into the model in an attempt to emulate the approach from DNS and LES models that use larger domain sizes and solve the equations for the turbulent fluid flow on a grid. Even though the effects of introducing this heterogeneous space setup into PARCELY are

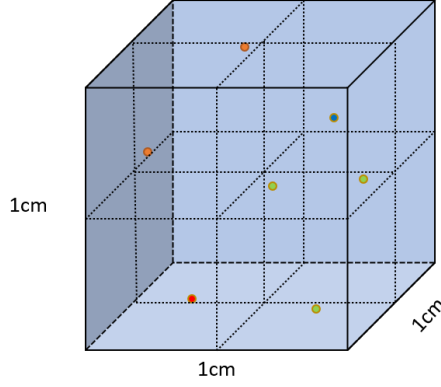


Figure 15: Graphical depiction of the gridded version of the PARCELY model, assuming a 1 cm^3 domain size. The colored circles represent different droplets, and the domain has been split 8 subdomains.

limited due to the much smaller domain size and neglecting the dynamical aspect of turbulence (the velocity components), the comparison of the results with output from the more advanced and rigorous models may aid in determining which processes are important, and at what scales.

To do this, the parcel domain can be subdivided into cubes of equal volumes, each with their own evolving value for saturation ratio, temperature, and pressure. The thermodynamic equations involving saturation ratio metrics are slightly modified in order to allocate the particles to the cube that they are residing in at each time step. At any instant, each subdomain can have n number of droplets within, where n is the set of non-negative numbers up to the total number of droplets simulated. Thus, the sink term of environmental saturation in Eq. (6) can often be zero (i.e, no droplet in the subdomain), depending on the number of particles in the total domain, their size, and their velocities. To more accurately simulate such a system, the diffusion of water vapour and temperature between adjacent subdomains is included and calculated using a discretized form of the diffusion equation:

$$\frac{dS}{dt} = D \nabla^2 S \quad (29)$$

$$\frac{dT}{dt} = \alpha \nabla^2 T \quad (30)$$

where D and α are the diffusivity of water vapour and thermal diffusivity of air ($\text{m}^2 \text{s}^{-1}$). The former is defined in section 2.1.2 and the latter is defined as

$$\alpha = \frac{k_a}{\rho_a c_p}. \quad (31)$$

The saturation ratio and temperature fields are initialized as monotonic fields, so that they all begin with the same value. The boundaries, i.e. the outer subdomains, are set equal to their nearest neighbouring subdomains prior to solving the equation at each time-step. This is done to give the illusion of the parcel existing within a larger field or domain. As an example, if

we wished to simulate a pocket of comparably dry air in a corner of the parcel, having the effects on temperature or saturation ratio ripple immediately to the opposite corner would not be representative of the actual diffusion processes occurring.

Particles are uniformly and randomly distributed throughout the domain, and allowed to overlap in their position since collisions and inter-particle considerations are ignored entirely (see section 2.1.1). Their horizontal velocities are also uniformly (and randomly) distributed between $\pm 0.05 \text{ cm s}^{-1}$, although this is highly unrealistic. In reality, small particles and droplets will move with the air flow dominated by the dissipative and inertial-range eddies at these scales, which is turbulent and random. In contrast to reality, in our setup the particles move in a billiard-ball like motion, meaning they are initialized with a random horizontal velocity (vertical velocity is still equal to the updraft velocity, while taking into account the terminal velocity) that they retain throughout the model run. The particles can cross subdomains, and we apply periodic boundary conditions to all faces of the cubic domain, so that any particle going through one side comes out the opposite with the same velocity. The effect of changing the particle dynamics is considered in this experiment to a limited degree by keeping them in fixed positions, as will be further discussed below.

3.2.2 Results

Firstly, we use the mono-disperse aerosol distribution to test the impact of changes in grid resolution (i.e., the number of grid boxes) and domain size on the saturation ratio. We run the model using domain sizes ranging from $1\text{--}5 \text{ cm}^3$ and grid resolutions ranging from 2^3 – 6^3 subdomains. The results are shown in Figures 16 and 17. In both figures the standard deviation of supersaturation (using all the subdomains) is given over time, where the subplots of Fig. 16 are runs with the same domain size, and the latter with the same grid resolution. The peak value of standard deviation of supersaturation is over 0.08, for the 2^3 grid in the 5 cm^3 domain. This magnitude agrees well with the values from the manuscript from Thomas et al., however qualitatively the agreement is lacking.

Thomas et al.’s supersaturation standard deviation displays a well-defined peak near the time of activation of most droplets, followed by a gradual sloping decrease to a lower steady-state value. In Fig. 16 we see peaks in the 2 and 5 cm^3 domain sizes, but less clearly in the others. In addition, the former peak is shifted in time to the right of activation, which occurs between 70 s and 80 s in the simulation. It is possible that this is simply an averaging issue, since Thomas et al. use a DNS model with 128^3 grid points representing 1 cubic millimeter volumes and the fluctuations are smoothed out substantially when averaged. However this does not explain why the peak is found here using the 5 cm^3 domain size, but not for all the others. When performing the same test with a 1 cm^3 and 10^3 subdivisions (in order to have the same gridbox volume as in Thomas et al.), we find no clear peak in the standard deviation.

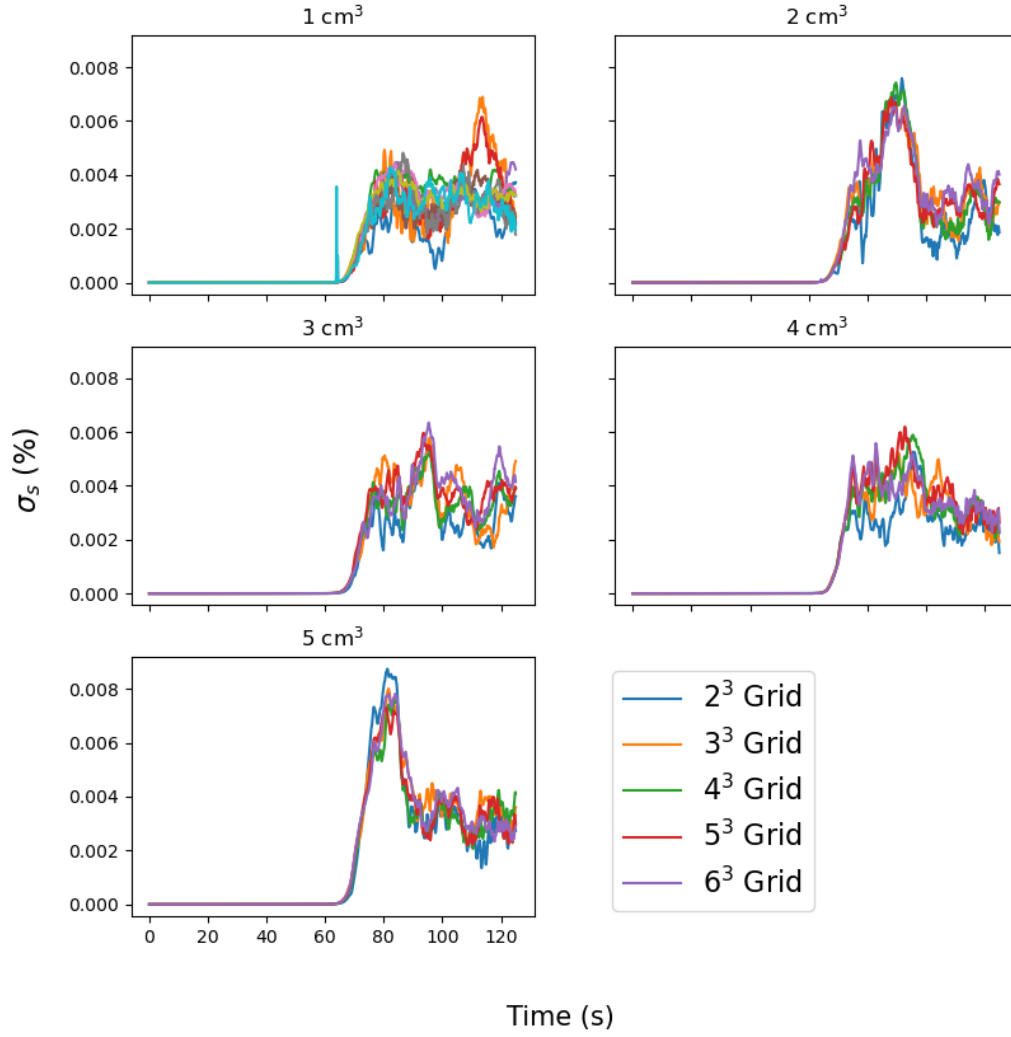


Figure 16: Standard deviation of supersaturation (σ_s) over time, with each subplot showing runs of the same domain size in cm^3 but of different grid resolution (e.g. 2^3 Grid is a domain subdivided into 2^3 equal-volume subdomains). Every model run uses the mono-distribution described in Table 1.

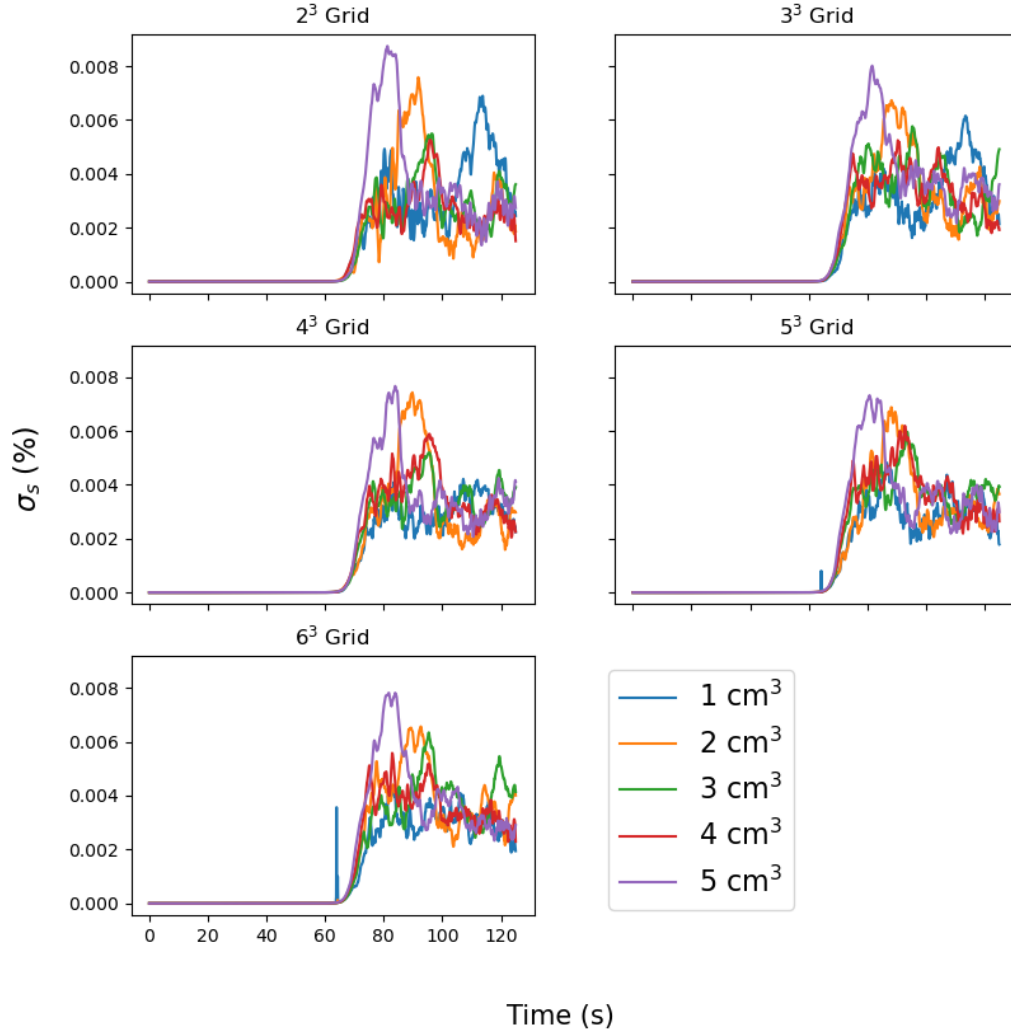


Figure 17: Standard deviation of supersaturation over time, where each subplot showing runs with the same grid resolution but different domain size. Every model run uses the mono-distribution described in 1.

Additionally, the same figure was recreated using different random generator seeds instead of using the same in each model run. Therefore, the randomly uniformly distributed horizontal velocities would be different for each run. This test removes the well-defined peaks in the 2 and 5 cm^3 domain sizes, returning more random behaviour at droplet activation as in the other domain subplots of Figs. 16 and 17. This points to the coupled air flow and droplet dynamics as a potentially important factor in the evolution of the supersaturation inside an air parcel, although not to a critical extent for the domain sizes and droplet number concentration tested here.

Despite the issue of resolving a peak in the standard deviation of supersaturation near activation, we see that there is no substantial difference in behavior when taking into account different domain sizes and grid resolutions. Every droplet activates at nearly the same time throughout every test run, at least to within 0.2 seconds (time-resolution of the data that had

been pre-defined). This is unsurprising due to the size of the domain (though also due to the monodisperse aerosol) and the speed at which the water vapour diffuses among neighboring grid boxes; pockets of high or low supersaturation don't have the time to form since they will either quickly have a droplet in their area, acting as a sink (or source) of water vapour, or diffuse quickly to their neighbours which dampens their fluctuations. When applying a 5^3 grid to model runs with a pristine or polluted aerosol size distribution, there is little to no difference in activation count over time, limited to at most a discrepancy of one or two activated droplets at any given point.

While the introduction of a saturation ratio and temperature grid does little to change the results of our simulations as compared to a result with a single value for both variables in the entire domain, it is important to reiterate that the employed approach completely neglects the impact of the turbulent velocity field on the evolution of the droplets. When subdividing the domain, the dynamics of the particles becomes important as well. Droplets caught in a turbulent eddy could be separated from the population and temporarily exposed to a different environment (perhaps an eddy of comparably drier air for example). Thus, we also need to look into how altering the positions and velocities of the particles within a subdivided domain can affect the simulation.

As an initial test, we compare the results of a model run of the mono-disperse distribution with a homogeneous field, a heterogeneous field, and a heterogeneous field in which the droplets are only located in one “corner-column” of the domain (a vertical stack of subdomains; an example can be seen in Fig. 18a) and not allowed to move in the horizontal, as opposed to being uniformly distributed throughout the domain. It is important to note again that the periodic boundary conditions do not apply to the diffusion of saturation ratio; the subdomains in one corner do not “see” what a subdomain in an opposite corner experiences. Figure 19 shows all the supersaturations in each subdomain over time in the left plot. Immediately it can be seen that there is a much larger spread of values in the corner run compared to the uniform distribution, which can also be seen in the difference in standard deviation displayed in the center plot (roughly by an order of magnitude).

There are two discernible groups of corner-run supersaturations: the smooth group that have the highest levels of supersaturation (above the homogeneous supersaturation line) and only experience the source term from the saturation ratio evolution equation driven by the updraft, and the “wiggly” group that are situated on or below the homogeneous supersaturation line that experience both the source updraft term and the sink condensation term. Without the incorporation of diffusion, the smooth group would continually increase for the entire run, and the “wiggly” group would likely be exhibiting even lower values of supersaturation.

The effect on the droplet sizes can be seen in the final plot of Fig. 19, where all droplet radii are plotted. Once again, there is a marked difference between the two runs, this time in the size distribution. The spread in the corner-run at the final time-step is roughly half a microm-

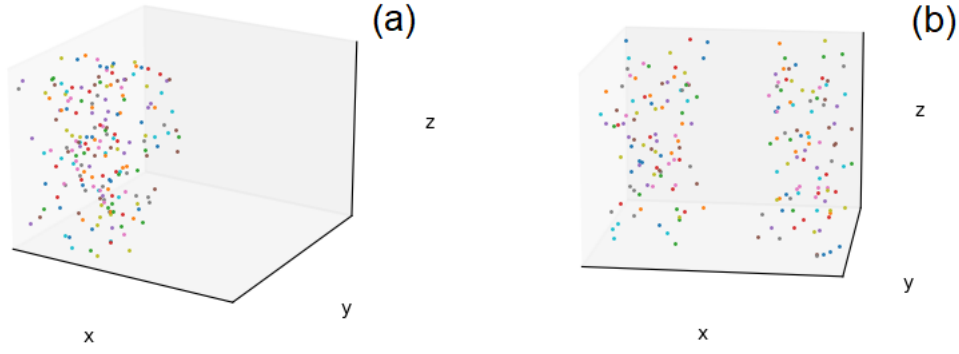


Figure 18: Schematics of the “corner-column” (a) and x-axis horizontal split (b) droplet positions used for testing the influence of position on the saturation ratio field.

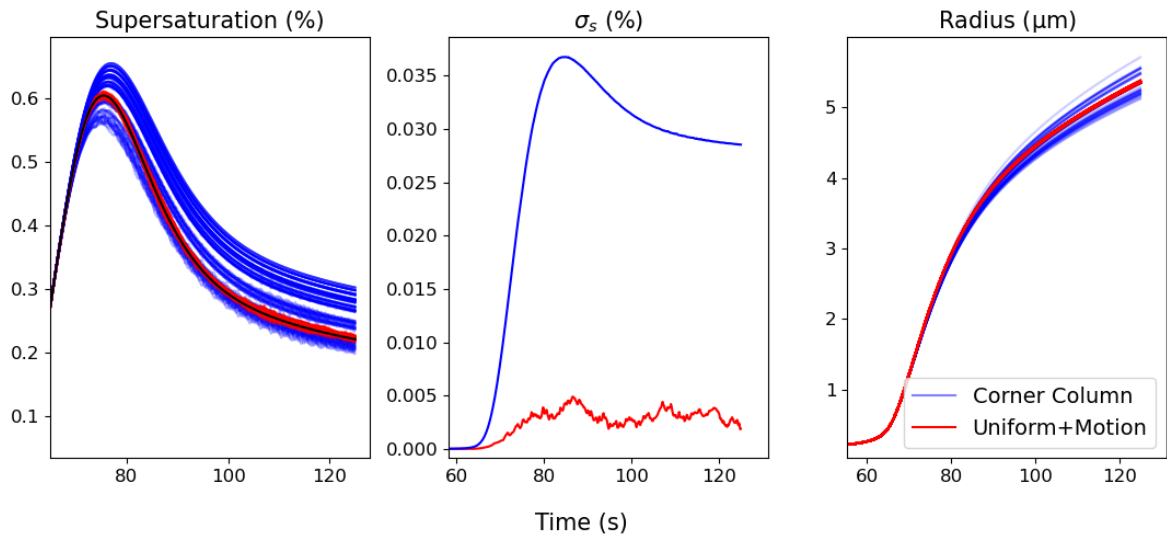


Figure 19: Supersaturation (left), standard deviation of supersaturation (center), and mean droplet radius (all droplets) for homogeneous (black), heterogeneous (125 lines, red), and heterogeneous-cornered (125 lines, blue) model runs using the mono-disperse distribution described in 1.

eter, while for the uniformly distributed run it is roughly 0.03 micrometers- again an order of magnitude difference. There is a small but noticeable clustering effect on the corner-run radii as well; this is due to their positions, which randomly places them inside subdomains that they remain in throughout the simulation. Thus, droplets within the same subdomain(s) will tend to have the same environment and similar evolution.

While it is clear from this figure that there is a significant impact on the size distribution, all of the droplets have obviously activated as in the homogeneous case. We perform a similar test with the pristine and polluted distributions, where we again constrain the droplets to one corner column of the domain, and another where we separate the two contributing log-normal populations of the distributions along the x-axis (Fig. 18b). The results of these tests, compared to the homogeneous and heterogeneous model runs are shown in Figures 20 and 21.

Looking first at the fraction of activated droplets in Figure 21, we see that the effect of parti-

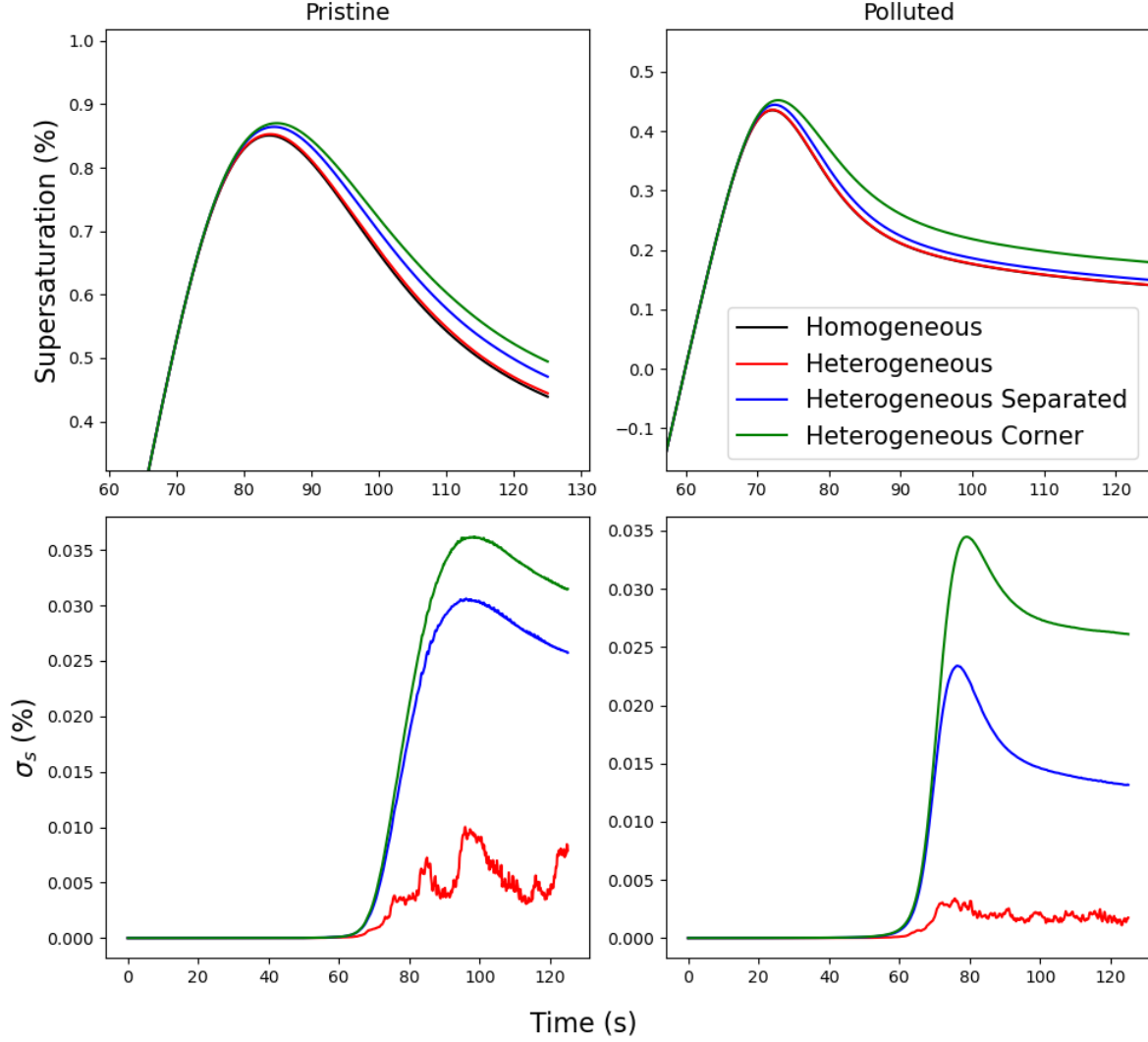


Figure 20: Supersaturation and standard deviation of supersaturation for pristine and polluted aerosol size distributions, comparing model runs with a homogeneous and heterogeneous saturation ratio and temperature fields, as well as heterogeneous fields where the particles are either kept in a corner column of the domain, or the lognormal populations contributing to their bi-modal distributions are separated along the x-axis.

cle positioning is negligible for the pristine distribution. The separated run returns the same activated fraction as the pure-heterogeneous and homogeneous runs, while the corner run is essentially identical. The effect on the polluted distribution is more noticeable, with a 3% difference between the separated run which produced more activated droplets than the homogeneous and heterogeneous runs, and the corner run which produced fewer. These variations are within the range for natural internal variability within the model, so the experiment needs to be performed with several different generator seeds to prove that this is statistically significant.

In addition to having fewer activated droplets, the corner run also has a smaller mean radius for the activated droplets compared to the pure homogeneous or heterogeneous runs, also in Fig. 21. The separated run has a smaller mean radius as well, although the difference is minor. The results are qualitatively the same for the pristine distribution. While the mean supersatu-

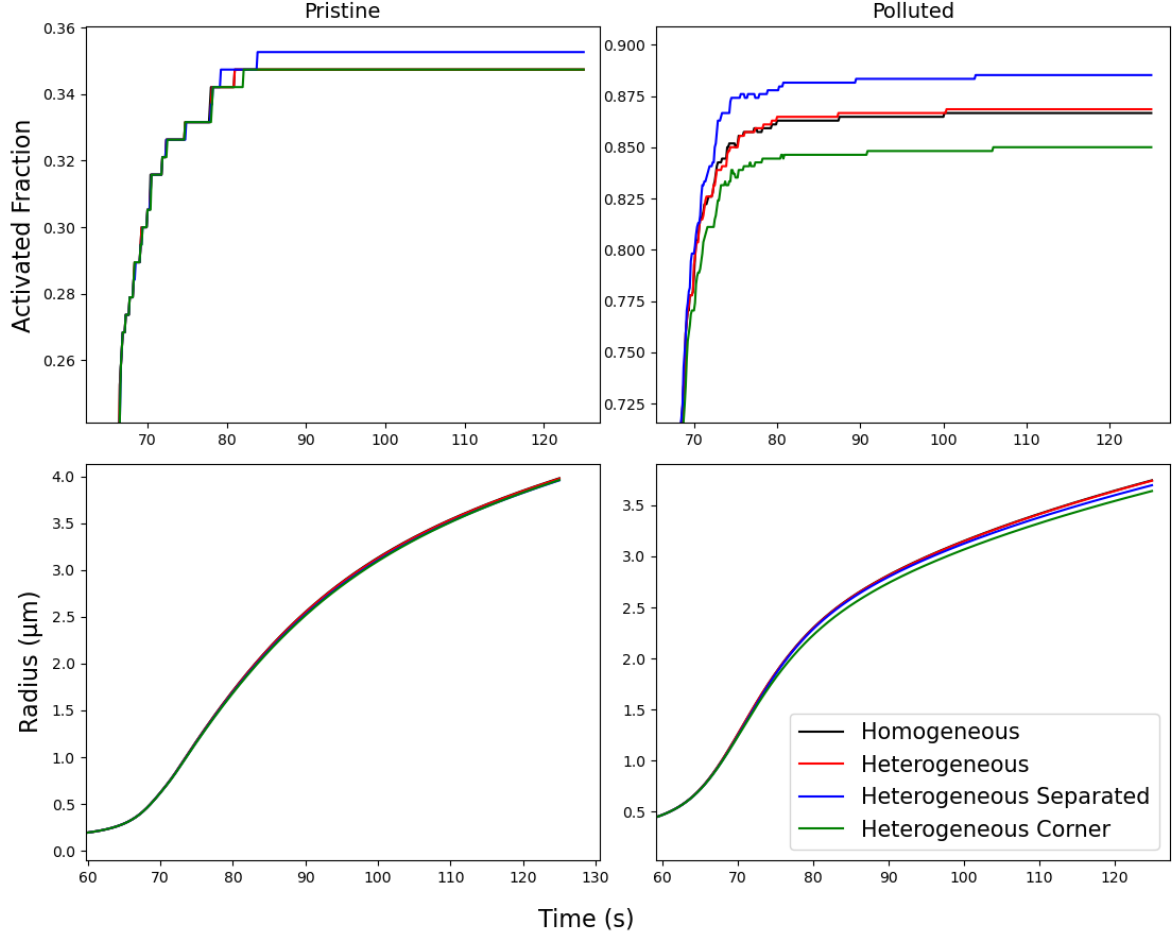


Figure 21: Activated fraction and mean droplet radius for pristine and polluted aerosol size distributions, comparing model runs with a homogeneous and heterogeneous saturation ratio and temperature fields, as well as heterogeneous fields where the particles are either kept in a corner column of the domain, or the lognormal populations contributing to their bi-modal distributions are separated along the x-axis.

rations in Fig. 20 show higher values for the separated and corner model runs, this is not the full picture. Much like in Figure 19, for both runs the set of unexposed subdomains have a much higher supersaturation than the mean in the pure homogeneous or heterogeneous runs, while the exposed subdomains have values equal to or lower than the pure homogeneous or heterogeneous runs. Thus, it is necessary to look once again to the standard deviation of the supersaturation in Figure 20 where it can be seen that the corner run returns the highest standard deviation, but comparable in magnitude to the separated run. As with the mono-distribution test, the pure heterogeneous standard deviation is an order of magnitude smaller.

3.2.3 Discussion

In this experiment, we implemented a spatial subdivision of the PARCELY model's domain for saturation ratio and temperature to see how having a heterogeneous field differs from a single-value homogeneous one, and to gain insights into how it might help inform about and interpret future comparisons with LES and DNS models. Importantly, this approach does not

simulate or resolve any turbulent motion and variable fields, but rather quantifies the spatial differences in saturation ratio and temperature as a result spatially separated variations in the thermodynamics (primarily saturation ratio) inside the cloud parcel (absent any consideration of turbulent or laminar mixing) and how those spatial inhomogeneities affect droplet growth. This approach could possibly be used as a proxy for a turbulent parcel in the future, however due to the limitations in parcel volume and the size of the relevant eddies impacting droplet growth, this is unlikely.

While the implementation returns standard deviations in supersaturation similar in magnitude to the results from a DNS model, this approach fails to consistently recreate the peak in standard deviation that occurs at activation, and thus neither the subsequent decrease to a steady value post activation. We speculate that this could be due to the much larger domain and particles used in the DNS model, which likely smooths out the profile through averaging. We also saw that the results are heavily dependent on the initial “billiard-ball” velocities of the particles set by the seeded pseudo-random number generator. This suggests that perhaps the turbulent or eddy-driven droplet dynamics may play a part in determining the standard deviation profile. In addition, the gridded version of the model had no effect on activation and a negligible effect on droplet size for the mono-distribution as well as the pristine and polluted ones.

We investigated the role of droplet position inside the parcel on droplet and saturation ratio evolution by placing all droplets inside one corner column of the parcel. This predominantly affects saturation ratio, creating two regimes of values: those for subdomains housing droplets with saturation ratio equal or less than the homogeneous saturation ratio, and those for subdomains without droplets that are denied continuous growth due to diffusion of water vapour, but can still have saturation ratio values around 0.1 % higher than the affected subdomains’ saturation ratio. This leads to a segregation of the monotonic radius according to subdomains, resulting in differences in final radius (at 200 s simulation time) of around 0.5 micrometers. The corner-positioning test was performed on the pristine and polluted distributions, as well as a test in which the populations were split roughly by size on the x-axis. Both cases returned minimal influence on mean droplet size and activated fraction, only reproducing the increase in saturation ratio standard deviation. The effects are more pronounced for the polluted distribution, likely due to the larger aerosol number concentration.

4 Results: Co-condensation and Organic Films

Topping et al., 2013 performed numerous parcel model tests with varying parameters and variables, such as the updraft velocity, total organic content, and aerosol size distribution. Here, we only use their simulation shown in their Figures 1 and 2 to analyze the effects of adding organic films to the aerosols. It is important to reiterate here that the following simulations include both consideration of co-condensation of organic compounds, whose vapour pressures are represented by a volatility basis set, as well as the formation of an organic film impacting the (evolving) surface tension as particles grow due to water uptake and organic co-condensation – see description of the implementation of these features in Section 2.1.3. The total and condensed organic content is visually estimated from their Figure 2, and so a perfect replication of initial conditions is untenable. In addition, a constant surface tension of 0.04 J m^{-2} is assigned to all the organic components in the simulation. This will lead to a droplet’s surface tension being at that value while a complete organic film is possible (given the finite volume limitation of covering the surface by a limited amount of organics), while our model includes the evolution of surface tension toward the value of pure water once the organic surface film only partially covers the droplet.

PARCELY’s initial conditions to recreate the total organic content and partitioning from the Topping et al., 2013 simulation are shown in Table 6, derived from the method detailed at the end of Section 2.1.3. Figure 22 shows the evolution of supersaturation over time, activated droplet radius, number of activated droplets over time, and the final size distribution after 200 s of the droplets for the conditions emulating the simulations by Topping et al., 2013 with and without using organic films.

Table 6: Initial organic mass contents for the simulations emulating the run from Topping et al., 2013.

Saturation Concentration ($\log_{10} C^*$)	Condensed Mass Fraction (%)	Total Condensed Mass ($\mu\text{g m}^{-3}$)	Vapor Mass ($\mu\text{g m}^{-3}$)	Total Mass ($\mu\text{g m}^{-3}$)
-6	11.818	2.277	0	2.277
-5	9.799	1.888	0	1.888
-4	10.895	2.099	0	2.099
-3	14.174	2.731	0	2.731
-2	12.254	2.361	0	2.361
-1	12.177	2.346	0	2.346
0	5.226	1.007	0	1.007
1	2.16	0.416	0	0.416
2	≈ 0	≈ 0	0.48	0.48
3	≈ 0	≈ 0	1.18	1.18

Despite the inexact initialization, the supersaturation and activated droplet count for the pure-water surface tension run (black lines) match the original simulations well (not shown, see

Topping et al., 2013 Fig. (1)), and so we are confident that the inter-model comparison here is valid. Following this, employing the organic film mode for an evolving surface tension computation, the peak supersaturation is lowered by roughly 0.03 %, and the number of activated droplets increased to near 100 % (294/300, 26 extra activated droplets). The link between the peak supersaturation and number of activated droplets can be noticed in the mean radius, which is smaller than in the pure-water run. Because more droplets activate in organic film mode, more water vapour is more efficiently absorbed and consequently, the bigger droplets do not grow as large as they do without the organic film, thus lowering the mean radius and the peak supersaturation.

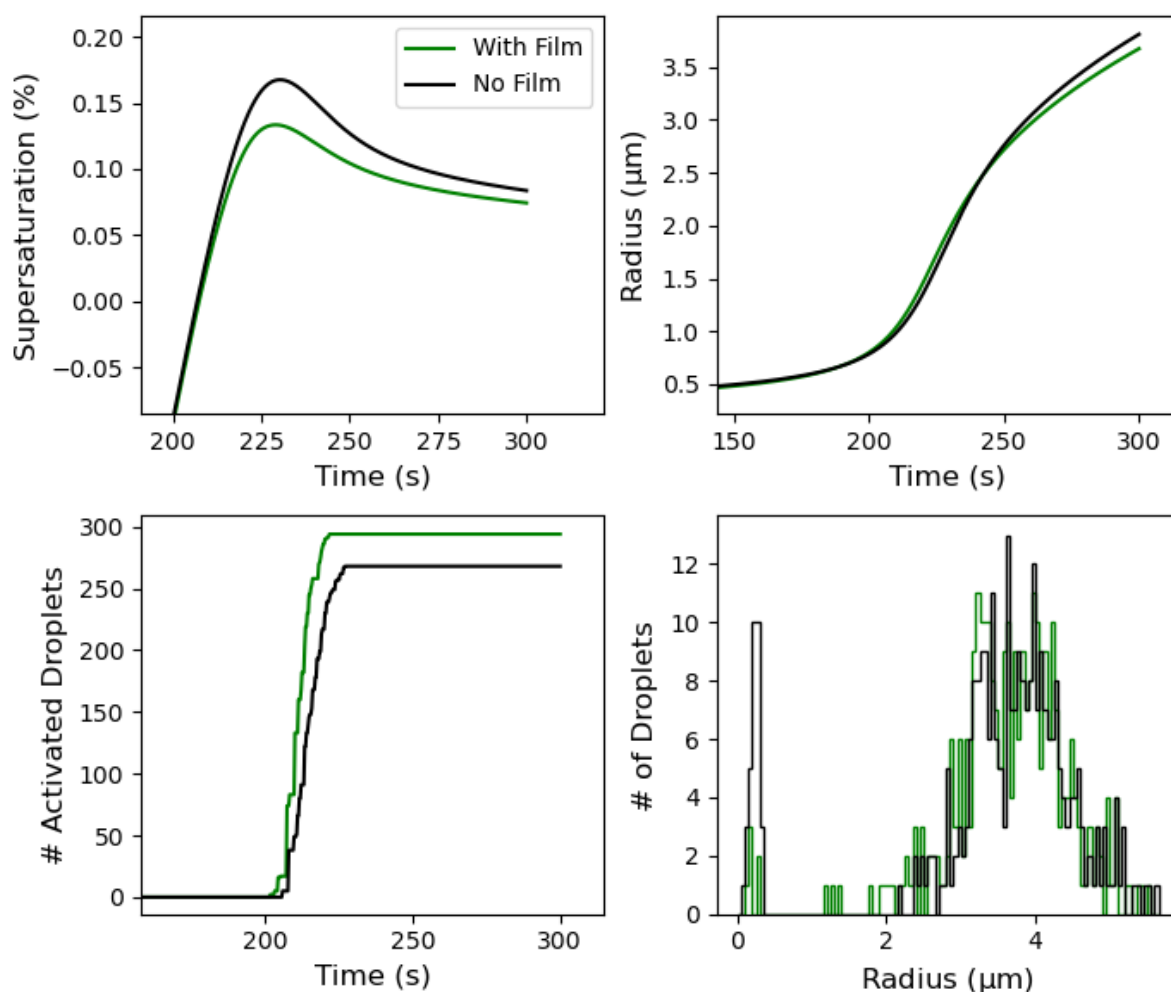


Figure 22: Results from PARCELY's simulations using the initial conditions from Topping et al., 2013, Figures 1 and 2. The green curves represents the run with organic films, and the black curves represents with the surface tension of water (as a function of temperature). Both include co-condensation.

Looking at the solute data, Fig. 23 (a) shows the final droplet radius (wet radius) over the initial solute radius (dry radius) for both simulations. It can be seen that the critical initial dry solute radius for CCN activation is larger for the 'no film' case. Fig. 23 (b) shows the difference in the final solute (dry particle) radius between the simulation with an organic film and the simulation without. The organic film method has the effect of growing the smallest solutes at the expense

of the largest ones, which are slightly smaller in the organic-film run compared to the pure-water run. This has a knock-on effect on the droplet radius. Bigger droplets will allow for more co-condensation to occur, thus increasing the solute mass and radius. The solutes with radii in the range between roughly 50 and 80 nm are the ones that are additionally activated in the organic-film mode.

After performing the same test for varying updraft velocity between 0.1 and 1 m s⁻¹ and inorganic mass fraction of the solute between 10 and 90 %, for both pure-water and organic film surface tensions, the latter was found to have a negligible effect for aerosol size this distribution and these initial conditions on peak supersaturation, droplet activation, or mean activated radius. Incorporating organic films primarily had a shifting effect on droplet activation count, allowing for more droplets to activate, especially at lower updraft speeds.

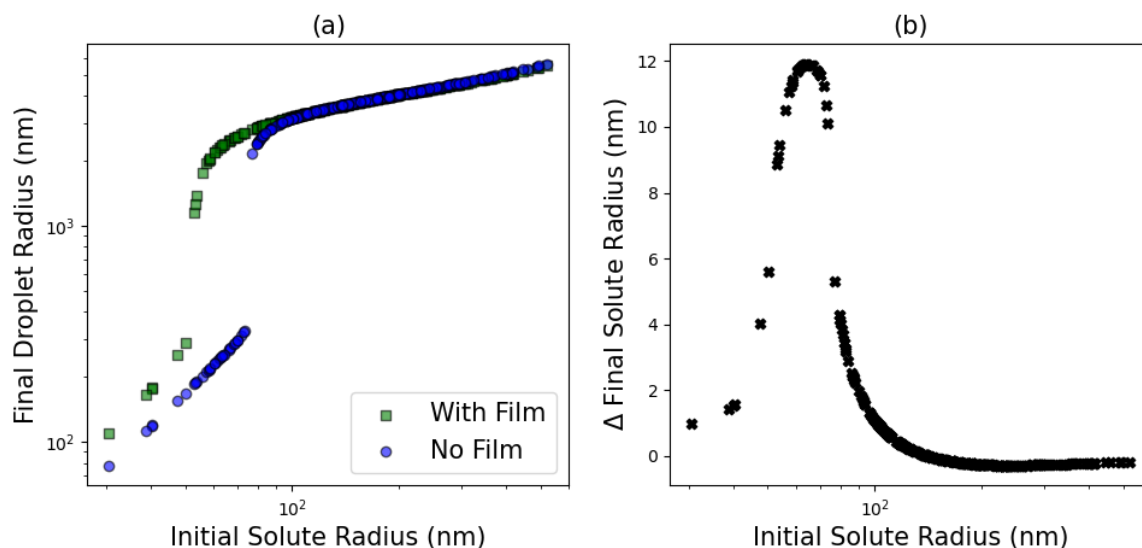


Figure 23: Scatter plot of (a) the final (wet) radius over the initial solute (dry particle) radius for the Topping et al., 2013 simulation with (green) and without (blue) organic-films, and (b) the difference in final solute radius between the two simulations over the initial solute radius. Notice the logarithmic scale for (a) and the linear scale for (b) on the y-axes. Here, the final radius is taken after 200 s simulation time.

To further evaluate the impacts of co-condensation and organic films, the pristine and polluted size distributions and associated initial organic mass distributions from Table 1 are run with different configurations of co-condensation and organic film mode: off or on for either process, resulting in four combinations. In addition, two updraft velocities – 1 and 0.3 m s⁻¹ are tested, resulting in a total of 16 model runs. The organic mass concentrations and initial condensed-phase mass fractions are set-up for both distributions, using the same initial total concentrations are given in Tables 7 and 8. The resultant condensed organic mass is calculated and subtracted from the total concentration to determine the vapour concentration.

Due to the change in the number of particles present, this results in an unrealistic amount of low-volatility organics in the vapour phase present in such high relative humidity for the

Table 7: Initial organic mass contents for the pristine distribution simulations. Note that Condensed Mass Fraction is for the whole solute (including inorganics), so will not sum to 100 %.

Saturation Concentration ($\log_{10} C^*$)	Condensed Mass Fraction (%)	Total Condensed Mass ($\mu\text{g m}^{-3}$)	Vapor Mass ($\mu\text{g m}^{-3}$)	Total Mass ($\mu\text{g m}^{-3}$)
-6	6.166	0.019	0.081	0.1
-5	5.113	0.016	0.084	0.1
-4	5.685	0.017	0.083	0.1
-3	7.396	0.022	0.098	0.12
-2	6.394	0.019	0.101	0.12
-1	6.354	0.019	0.101	0.12
0	2.727	0.008	0.142	0.15
1	1.127	0.003	0.237	0.24
2	≈ 0	≈ 0	0.48	0.48
3	≈ 0	≈ 0	1.18	1.18

Table 8: Initial organic mass contents for the polluted distribution simulations.

Saturation Concentration ($\log_{10} C^*$)	Condensed Mass Fraction (%)	Total Condensed Mass ($\mu\text{g m}^{-3}$)	Vapor Mass ($\mu\text{g m}^{-3}$)	Total Mass ($\mu\text{g m}^{-3}$)
-6	6.166	0.115	0	0.115
-5	5.113	0.096	0.004	0.1
-4	5.685	0.106	0	0.106
-3	7.396	0.138	0	0.138
-2	6.394	0.12	0	0.12
-1	6.354	0.119	0.001	0.12
0	2.727	0.051	0.099	0.15
1	1.127	0.021	0.219	0.24
2	≈ 0	≈ 0	0.48	0.48
3	≈ 0	≈ 0	1.18	1.18

Pristine case. All runs for each distribution begin with the exact same initial conditions and aerosol configurations. Unlike the Topping et al., 2013 comparisons, here the molar mass for each organic species descends in evenly-spaced increments from 400 g mol^{-1} for the lowest-volatility species to 200 g mol^{-1} for the highest. Molar mass tends to decrease with increasing volatility/saturation concentration and can vary around 50 g mol^{-1} on the low end (Lannuque et al., 2018), but we decided to limit the range for simplicity.

Figure 24 shows the number of activated droplets over time for all model runs. Our attention is immediately drawn to the pristine runs with both effects (blue), where the combination leads to nearly triple the amount of activated droplets. This is in contrast to the polluted panels, where the increase is not as dramatic, percentage-wise, although still results in the highest number of activated droplets, while those with neither effect considered (red) return the fewest. It is evident how the organic vapour content is important in determining the relative contribution to

activation when comparing the position of the runs with only organic films (green) and those with only co-condensation (orange) between the pristine and polluted cases. Where there is more organic mass available for co-condensation in the former, co-condensation results in more activated droplets by increasing the solute mass. In the latter case in which most of the organic content is already condensed, the organic films subsist and therefore depress the surface tension for a longer time, encouraging more droplets to activate.

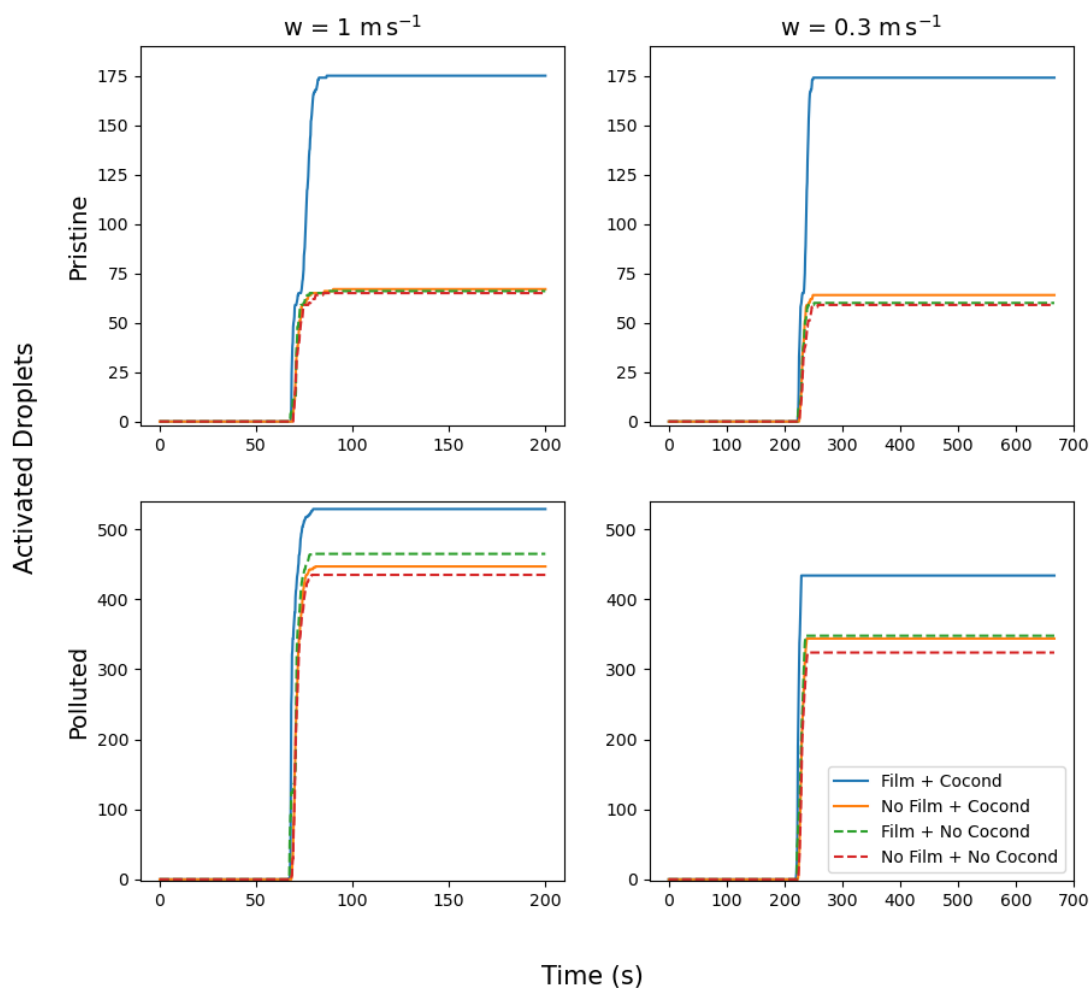


Figure 24: Number of activated cloud droplets over time for 4 configurations of co-condensation and surface tension for a pristine and polluted aerosol distribution, and 1 m s^{-1} or 0.3 m s^{-1} updraft velocity. Here, 'No Film' implies the use of the surface tension of pure water as a function of ambient temperature. The pristine case has a total CCN count of 190, while the polluted case has 540.

Figures 25 and 26 show the final droplet radius distribution and the mean activated droplet radius respectively. We see that in all cases the runs with both co-condensation and organic films lead to a smaller mean activated droplet radius as was similarly shown for the comparison with the Topping et al., 2013 initial conditions. There is no noticeable increase in size distribution for the pristine case, while the polluted case shows a slight increase in distribution towards the smaller sizes.

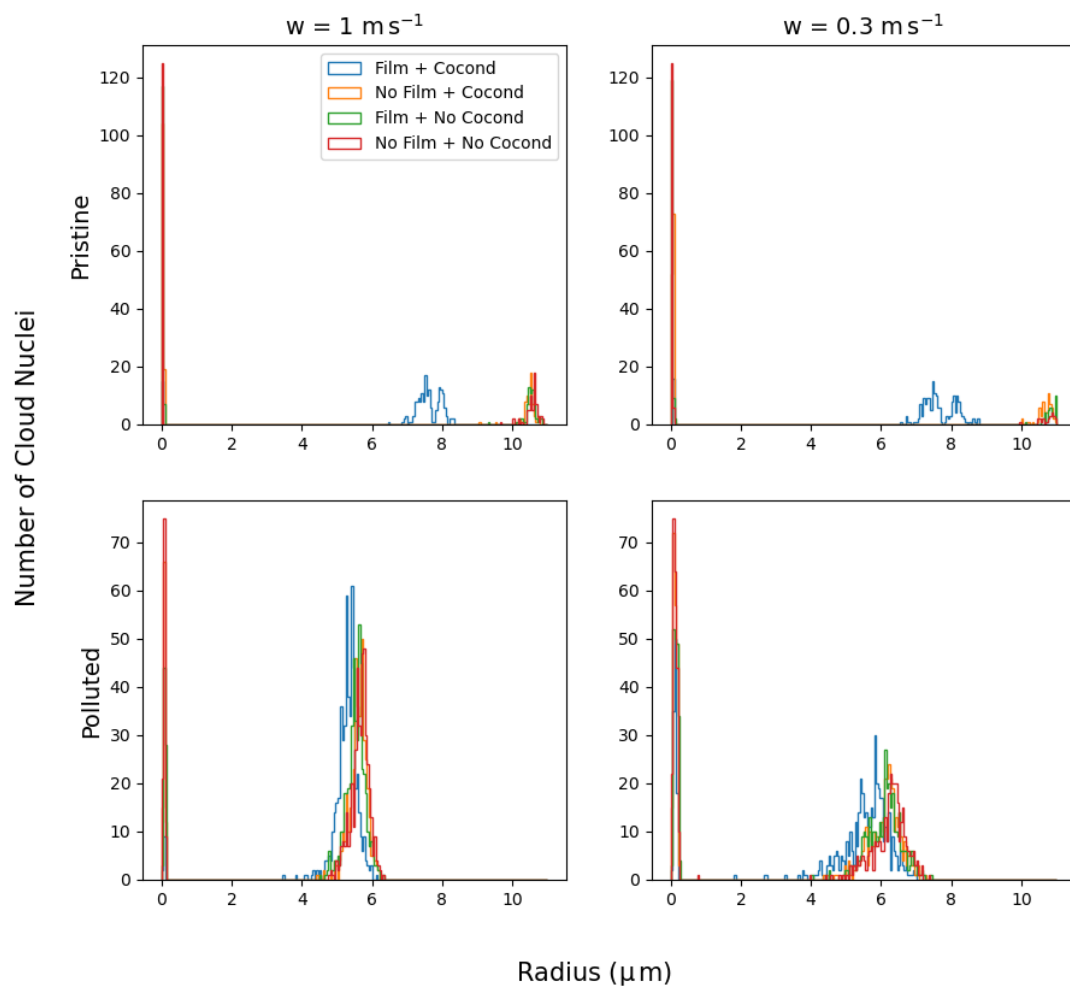


Figure 25: Histograms of the (wet) radius distribution at the final time-step (200 s) for the model runs described in Figure 24. The bin-width is set to $0.5 \mu\text{m}$.

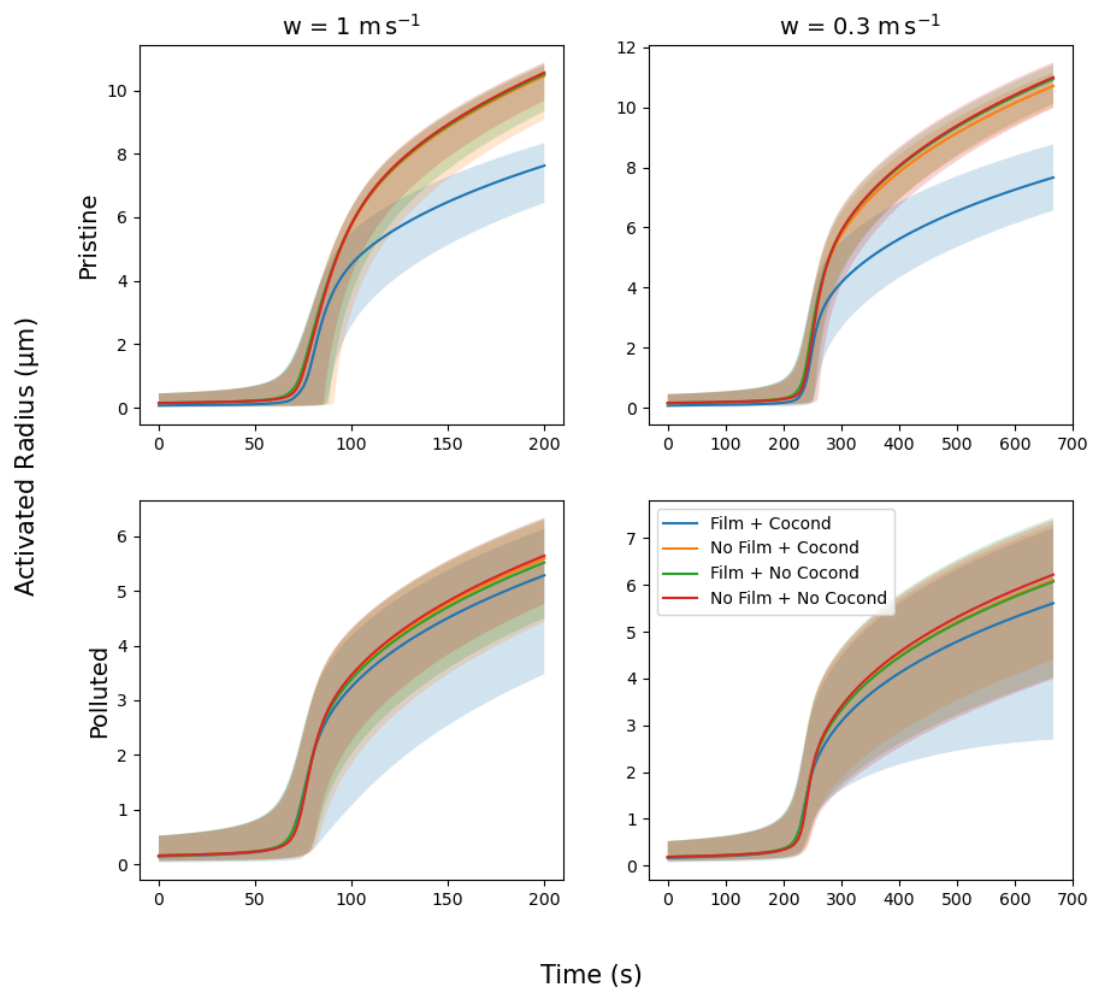


Figure 26: Mean activated droplet radius with maximum and minimum shading over time for the model runs described in Figure 24.

We perform the same simulations for the pristine and polluted distributions with varying updraft velocity from 0.1 m s^{-1} to 1 m s^{-1} and solute inorganic mass fraction ranging from 10 % to 90 %. Due to the change in inorganic mass fraction, the organic mass contents do not stay constant but vary slightly. One set of runs has both processes included, while the other considers only co-condensation. The results of peak supersaturation, activated droplet count, and mean activated radius are shown in Figures 27 and 28. Peak supersaturation is largely controlled by updraft velocity for both distributions, though a small inorganic mass fraction dependence can be seen from the tilt in gradient lines.

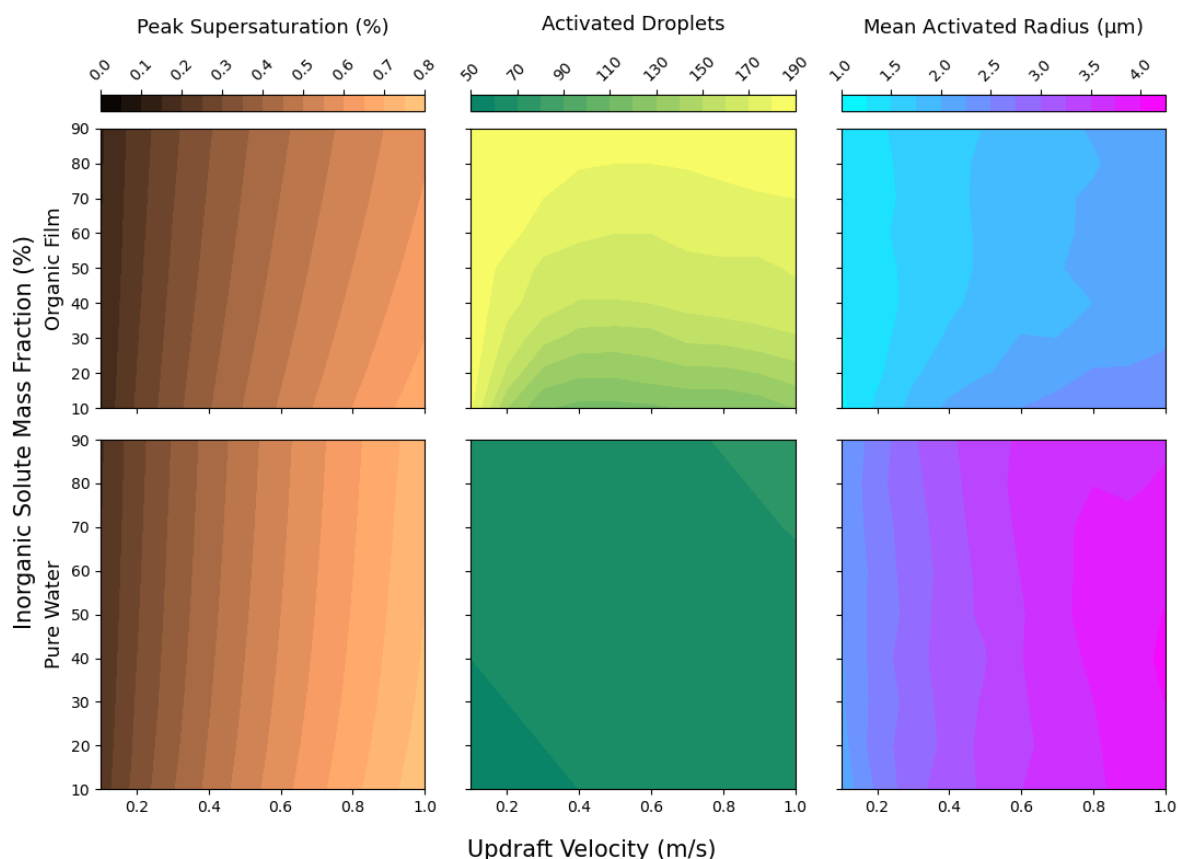


Figure 27: Peak supersaturation, activated droplet count, and mean activated radius at peak supersaturation for the pristine distribution run with co-condensation and organic films (top row) and only co-condensation (bottom row).

The polluted simulations' activation counts are largely identical both qualitatively and quantitatively; the organic film favors a higher count of activated droplets, which leads to a lower peak supersaturation and smaller activated radius at the moment of peak supersaturation as discussed previously. The pristine case however is much more interesting. Firstly, the number of activated droplets is largely dominated by inorganic mass fraction for updrafts larger than 0.2 m s^{-1} . Secondly, the number of activated droplets decreases with updraft velocity for low inorganic mass fractions until a certain point (for the range tested), and then increases. For example to 10 % inorganic mass fraction begins at 190 activated droplets for 0.1 m s^{-1} , decreases to 120 at 0.4 m s^{-1} , and then increases to 130 for updraft velocities above 0.6 m s^{-1} . This is

in contrast to what is seen in the polluted case and as generally expected. The reason for this is connected to the time it takes for co-condensation to occur, the organic-film, and the aerosol size distribution.

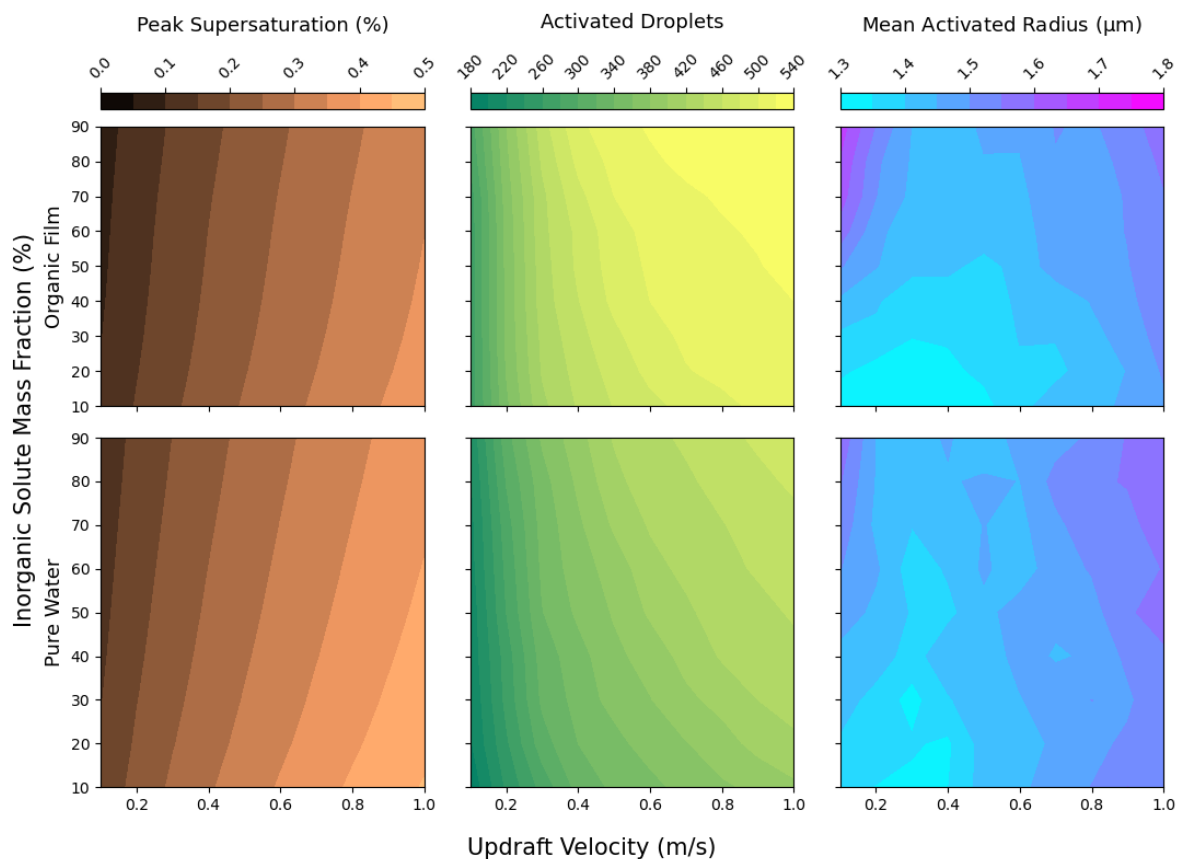


Figure 28: Peak supersaturation ratio, activated droplet count, and mean activated radius at peak supersaturation for the polluted distribution run with co-condensation and organic films (top row) and only co-condensation (bottom row).

In the case of the pristine distribution, a high updraft velocity disproportionately favors the larger aerosols, those most likely to activate even without the co-condensation and organic film effects considered. They will activate quickly given the fast updraft, and thus take up a larger share of both the water vapour and the organic vapour due to their increased size, leaving too little left for the smaller aerosols to get the boost required to activate. With slow updrafts, there is enough time for the smaller aerosols to still compete with their larger counterparts for their shares of the organics. This “levels the playing field” due to the increased mass and size of the smaller range of aerosols, resulting in most or all of aerosols activating and leading to a small mean droplet radius after 200 s of simulation time. If the aerosol distribution is too skewed towards larger aerosols, or has a larger number concentration, such as in the polluted case, the benefits of co-condensation taper off. Either the large aerosols remain too dominant, or there is too much competition for the same pool of total gas phase organic mass concentration, such that the added mass per aerosol is too small to have a substantial effect.

This cannot be the full explanation however; otherwise we would see some signal or similar result for the pristine runs without organic films. It seems that the benefits of co-condensation for the pristine runs aren't enough to activate the smaller droplets, and they are impeded by the relatively higher surface tension of pure water or simply their size. Lowering the surface tension by accounting for organic films removes that barrier by depressing the saturation ratio at the surface for all condensing species, not just water vapour. The solute and water mass growth rates are given additional support, thus unlocking the benefits of co-condensation for the pristine distribution.

Finally, we look at the mean activated radius at the moment of peak supersaturation. The reason moment of peak supersaturation is chosen over a specific time interval is due to the variation in updraft velocity. For example, analyzing after 100 seconds would result in runs with large updrafts being long past the moment of activation, while runs with small updrafts would not yet have activated most of their droplets (if at all). Selecting the moment of peak supersaturation removes this issue, but was not chosen for any other reason. It may be possible that a different time instance would have been more appropriate.

For the pristine distribution we have a familiar picture of updraft-dominated behavior for the pure-water-surface-tension run, with little influence by the inorganic solute mass. With organic films, similarly to its activated count plot, updraft velocity dominates at low speeds but inorganic mass becomes more important as the updraft speed increases, and returns higher mean radii. The explanation here is simple: larger updraft speeds yield higher supersaturation values, allowing for the aerosols to take up more water and grow larger within the simulation time period. Mean radius decreases with increasing inorganic mass fraction because the organic film "breaks" (meaning there is no longer enough organic matter to form a complete shell around the droplet, and the shell recedes) earlier since there is less organic mass to sustain it, thus the benefit of a low surface tension is lost earlier.

For the polluted distribution's mean activated radius we have a much noisier picture. Here inorganic mass fraction has the opposite effect: the mean radius increases with increasing inorganic mass fraction. There is too much competition for the reserve of organic vapours, and so the effects of co-condensation and organic films are muted in favor of size distribution effects. At low updraft speeds only the largest aerosols activate and control the mean activated radius. As the updraft increases, smaller aerosols are activated that bring the mean down, until the updraft velocity is large enough that there is enough condensational growth to increase the mean radius.

5 Conclusions

The modelling of clouds and their associated physics and dynamics has come a long way since the first computers used for climate and meteorological purposes were built in the 20th century. Yet even though we have improved both our theoretical understanding of cloud physics and our numerical and computational capabilities since the first bulk models were developed, in 2003 the parameterization of cloud microphysics in larger weather and climate models was still referred to as “a problem that refuses to die” (Randall et al., 2003). Therefore, it is imperative that the models used to derive, test, and improve these parameterizations, cloud parcel models, are suitably accurate and representative of the underlying microphysics.

This master’s thesis has introduced a new cloud parcel model, PARCELY. It is a particle-resolved air (cloud) parcel model coded entirely in Python and can be run easily without the need for excessive computational resources. The evolution of every aerosol particle is tracked within a set volume of air as it ascends with an updraft velocity. This framework blends approaches from both the computationally inexpensive but statistical method employed by bulk and bin models, and the computationally expensive but particle-tracking and high-resolution method of direct-numerical-simulation (DNS) models. However, in its current configuration PARCELY is made to focus only on the processes occurring during initial cloud formation and does not (yet) include hydrometeor interactions such as collision–coalescence or ice phase processes.

PARCELY can be expanded to include sub-domains for the environmental variables of saturation ratio, temperature, and pressure to emulate DNS even further, although proper implementation of droplet dynamics is not considered. Initial sensitivity tests show that this does not impact results significantly at the scales we run PARCELY ($1 - 10 \text{ cm}^3$). Additional sensitivity tests were performed on the mass and thermal accommodation coefficients as well, motivated by the longstanding lack of agreement on their values. We quantify the impact of their values (within a justified range) on the peak supersaturation with a normalized equation, and support the use of a value of 0.2 for both coefficients based on our analysis and the work from Raatikainen et al., 2013.

PARCELY has also been developed with the potential effects of organic compounds in mind. To address this, two key processes have been included: the formation of partial or complete organic films around particles that depress the surface tension, thus, encouraging droplet activation and co-condensation of organics onto the particles that alter the solute properties of the particle (size, hygroscopicity), further encouraging activation. To allow for easier consideration of non-homogeneous aerosol composition, PARCELY uses the κ -Köhler equation (Petters and Kreidenweis, 2007) instead of the van’t Hoff based Köhler version that is more commonly known.

While parcel models have already been developed or refined to include either organic films

(Lowe et al., 2019) or, very recently, co-condensation (Heikkinen et al., 2023), none have been made yet to include both, to our knowledge. With both effects considered, the processes compound to allow droplets that would normally be considered too small, to activate. This was shown in Figures 24, 27 and 28, with a substantial increase found for the pristine distribution that has both a low number concentration and smaller solute radii.

Given that any parcel of air that eventually becomes a cloud parcel is highly unlikely to be made up of purely clean air (i.e., only the fundamental components of Earth’s atmosphere: nitrogen, oxygen, etc.), the co-condensation and organic film processes would be persistently relevant for cloud formation. The increase in activated droplets alone is likely to have knock-on effects for collision-coalescence, and thus, the evolution of the droplet size distribution in the later stages of a cloud. We recommend that parameterizations of the initial cloud formation processes in larger models (LES, or cloud-resolving weather and climate models, for example) attempt to take into account the effects co-condensation and organic films.

It is highly unlikely that these larger models would be able to consider explicitly solving for the organic films as that would require detail in terms of organic material present in the cloud and its partitioning that is currently lacking. A parameterization of sorts would likely be the only computationally-acceptable way of incorporating the effects of co-condensation and organic films for now.

PARCELY will hopefully serve as a useful and accessible tool to anyone in need of a cloud parcel model for their research in the future. Its advantages lie in its ease of use and modification due to its simplistic coding in Python, as well as its more comprehensive approach to the modelling of aerosol processes that are vital to the determination of the most important output from cloud parcel models.

6 Future Work

There are many different research avenues one can explore using PARCELY as their tool of choice. Firstly, all non-comparison tests and simulations performed for this master’s thesis are limited in terms of the size distribution used for the aerosols (those defined in Table 1) and aerosol composition. Even though PARCELY currently includes parameters for 20 separate inorganic solute species, only ammonium sulphate was used in the example simulations shown in this work. Furthermore, all co-condensation and organic film runs use homogeneous values for the organics’ pure-component surface tension, density, and hygroscopicity. There is plenty of room for more testing using more realistic or observed ranges of values for these parameters.

Additional research can be done on the impact of the minimum thickness of the organic film, currently set at 0.3 nm (although a value of 0.2 nm is used in the text for comparison purposes), representative of the thickness of a water molecule. Non-ideal mixing via inclusion of activity coefficients could also be a fruitful avenue of exploration, to compare with the findings from Topping et al., 2013. Incorporation of complex but powerful approaches for mixing thermodynamics and surface tension (an extended version of the AIOMFAC model or the BAT model (Gorkowski et al., 2019) into PARCELY could also be an interesting avenue to determine the effects of rigorous thermodynamics on droplet activation in a parcel model.

While we do analyze how different updraft speeds can affect droplet activation when incorporating co-condensation and organic films, the range is only up to 1 m s^{-1} and does not include tests with an updraft varying over time. Further examination of the sub-domain version of PARCELY could also prove interesting if one is looking at the possible effects of entrainment and larger variations in supersaturation.

Furthermore, there is room for the inclusion of the microphysical processes ignored in the development of PARCELY and not included in the scope of this thesis, such as collision-coalescence, aerosol coagulation, or ice formation. These processes are complex and have no representation in PARCELY, but they are undoubtedly important to include in some form if one wishes to have a more comprehensive view of how all of the microphysics, processes, and sub-processes of clouds combine and affect the aerosol/droplet population that comprise them. A potential merging of an approach from a coagulation model with the PARCELY model has been discussed, to better represent conditions in either highly aerosol polluted environments or of longer time scale in the cloud stage to capture warm rain processes.

7 References

- Al-Abadleh, H. A. (2022). Atmospheric aerosol chemistry: State of the science.
- Alty, T., & Mackay, C. (1935). The accommodation coefficient and the evaporation coefficient of water. *Proceedings of the Royal Society of London. Series A-Mathematical and Physical Sciences*, 149(866), 104–116.
- Andrejczuk, M., Reisner, J., Henson, B., Dubey, M., & Jeffery, C. (2008). The potential impacts of pollution on a nondrizzling stratus deck: Does aerosol number matter more than type? *Journal of Geophysical Research: Atmospheres*, 113(D19).
- Barclay, P. L., & Lukes, J. R. (2019). Curvature dependence of the mass accommodation coefficient. *Langmuir*, 35(18), 6196–6202.
- Bellouin, N., Quaas, J., Gryspeerdt, E., Kinne, S., Stier, P., Watson-Parris, D., Boucher, O., Carslaw, K. S., Christensen, M., Daniaou, A. L., Dufresne, J. L., Feingold, G., Fiedler, S., Forster, P., Gettelman, A., Haywood, J. M., Lohmann, U., Malavelle, F., Mauritsen, T., ... Stevens, B. (2020). *Bounding global aerosol radiative forcing of climate change*. <https://doi.org/10.1029/2019RG000660>
- Bhowmick, T., & Iovieno, M. (2019). Direct numerical simulation of a warm cloud top model interface: Impact of the transient mixing on different droplet population. *Fluids*, 4. <https://doi.org/10.3390/fluids4030144>
- Carstens, J. C., Podzimek, J., & Saad, A. (1973). On the analysis of the condensational growth of a stationary cloud droplet in the vicinity of activation. *Journal of Atmospheric Sciences*, 31, 592–596.
- Chandrakar, K. K., Cantrell, W., Chang, K., Ciochetto, D., Niedermeier, D., Ovchinnikov, M., Shaw, R. A., & Yang, F. (2016). Aerosol indirect effect from turbulence-induced broadening of cloud-droplet size distributions. *Proceedings of the National Academy of Sciences of the United States of America*, 113, 14243–14248. <https://doi.org/10.1073/pnas.1612686113>
- Chen, S., Xue, L., & Yau, M. K. (2020). Impact of aerosols and turbulence on cloud droplet growth: An in-cloud seeding case study using a parcel-dns (direct numerical simulation) approach. *Atmospheric Chemistry and Physics*, 20, 10111–10124. <https://doi.org/10.5194/acp-20-10111-2020>
- Clark, T. L. (1973). Numerical modeling of the dynamics and microphysics of warm cumulus convection. *Journal of the Atmospheric Sciences*, 30, 857–878.
- Codoni, D. (2018). *Dns analysis of warm cloud microphysics and related mixing dynamic at the cloud-clear air interface* (Doctoral dissertation). Politecnico di Torino.
- Crooks, M., Connolly, P., & McFiggans, G. (2018). A parameterisation for the co-condensation of semi-volatile organics into multiple aerosol particle modes. *Geoscientific Model Development*, 11, 3261–3278. <https://doi.org/10.5194/gmd-11-3261-2018>

- Davidovits, P., Worsnop, D., Jayne, J., Kolb, C., Winkler, P., Vrtala, A., Wagner, P., Kulmala, M., Lehtinen, K., Vesala, T., et al. (2004). Mass accommodation coefficient of water vapor on liquid water.
- Davies, J. F., Zuend, A., & Wilson, K. R. (2019). The role of evolving surface tension in the formation of cloud droplets. *Atmospheric Chemistry and Physics*, 19(5), 2933–2946.
- Donahue, N. M., Robinson, A., Stanier, C., & Pandis, S. (2006). Coupled partitioning, dilution, and chemical aging of semivolatile organics. *Environmental science & technology*, 40(8), 2635–2643.
- Duplissy, J., DeCarlo, P. F., Dommen, J., Alfarra, M. R., Metzger, A., Barmapadimos, I., Prevot, A. S., Weingartner, E., Tritscher, T., Gysel, M., et al. (2011). Relating hygroscopicity and composition of organic aerosol particulate matter. *Atmospheric Chemistry and Physics*, 11(3), 1155–1165.
- Feingold, G., Stevens, B., Cotton, W., & Walko, R. (1994). An explicit cloud microphysics/les model designed to simulate the twomey effect. *Atmospheric Research*, 33(1-4), 207–233.
- Fountoukis, C., Nenes, A., Meskhidze, N., Bahreini, R., Conant, W. C., Jonsson, H., Murphy, S., Sorooshian, A., Varutbangkul, V., Brechtel, F., et al. (2007). Aerosol–cloud drop concentration closure for clouds sampled during the international consortium for atmospheric research on transport and transformation 2004 campaign. *Journal of Geophysical Research: Atmospheres*, 112(D10).
- Fukuta, N., & Walter, L. (1970). Kinetics of hydrometeor growth from a vapor-spherical model. *Journal of Atmospheric Sciences*, 27, 1160–1172.
- Gorkowski, K., Preston, T. C., & Zuend, A. (2019). Relative-humidity-dependent organic aerosol thermodynamics via an efficient reduced-complexity model. *Atmospheric Chemistry and Physics*, 19(21), 13383–13407.
- Grabowski, W. W., & Abade, G. C. (2017). Broadening of cloud droplet spectra through eddy hopping: Turbulent adiabatic parcel simulations. *Journal of the Atmospheric Sciences*, 74(5), 1485–1493.
- Grabowski, W. W., Andrejczuk, M., & Wang, L.-P. (2011). Droplet growth in a bin warm-rain scheme with twomey ccn activation. *Atmospheric Research*, 99(2), 290–301.
- Grabowski, W. W., Morrison, H., Shima, S. I., Abade, G. C., Dziekan, P., & Pawlowska, H. (2019). Modeling of cloud microphysics: Can we do better? *Bulletin of the American Meteorological Society*, 100, 655–672. <https://doi.org/10.1175/BAMS-D-18-0005.1>
- Grabowski, W. W., & Wang, L.-P. (2013). Growth of cloud droplets in a turbulent environment. *Annual review of fluid mechanics*, 45, 293–324.
- Heald, C. L., Ridley, D. A., Kroll, J. H., Barrett, S. R., Cady-Pereira, K. E., Alvarado, M. J., & Holmes, C. D. (2014). Contrasting the direct radiative effect and direct radiative forcing of aerosols. *Atmospheric Chemistry and Physics*, 14, 5513–5527. <https://doi.org/10.5194/acp-14-5513-2014>

- Heald, C. L., Kroll, J., Jimenez, J., Docherty, K., DeCarlo, P., Aiken, A., Chen, Q., Martin, S., Farmer, D., & Artaxo, P. (2010). A simplified description of the evolution of organic aerosol composition in the atmosphere. *Geophysical Research Letters*, 37(8).
- Heikkinen, L., Partridge, D. G., Huang, W., Blichner, S., Ranjan, R., Tovazzi, E., Petäjä, T., Mohr, C., & Riipinen, I. (2023). Cloud response to co-condensation of water and organic vapors over the boreal forest. *EGUsphere*, 1–42.
- Hinds, W. C. (1999). *Aerosol technology: Properties, behavior, and measurement of airborne particles*. John Wiley & Sons.
- Hodas, N., Zuend, A., Schilling, K., Berkemeier, T., Shiraiwa, M., Flagan, R. C., & Seinfeld, J. H. (2016). Discontinuities in hygroscopic growth below and above water saturation for laboratory surrogates of oligomers in organic atmospheric aerosols. *Atmospheric Chemistry and Physics*, 16, 12767–12792. <https://doi.org/10.5194/acp-16-12767-2016>
- Hsieh, W. C., Nenes, A., Flagan, R. C., Seinfeld, J. H., Buzorius, G., & Jonsson, H. (2009). Parameterization of cloud droplet size distributions: Comparison with parcel models and observations. *Journal of Geophysical Research Atmospheres*, 114. <https://doi.org/10.1029/2008JD011387>
- Jia, Y. (2020). *An investigation of the influence of the co-condensation of semi-volatile organics on cloud droplet number for various environments*. The University of Manchester.
- Kalova, J., & Mares, R. (2018). The temperature dependence of the surface tension of water. *AIP Conference Proceedings*, 2047. <https://doi.org/10.1063/1.5081640>
- Khain, A. P., Beheng, K. D., Heymsfield, A., Korolev, A., Krichak, S. O., Levin, Z., Pinsky, M., Phillips, V., Prabhakaran, T., Teller, A., Heever, S. C. V. D., & Yano, J. I. (2015). *Representation of microphysical processes in cloud-resolving models: Spectral (bin) microphysics versus bulk parameterization*. <https://doi.org/10.1002/2014RG000468>
- Khain, A. P., & Pinsky, M. (2018). *Physical processes in clouds and cloud modeling*. Cambridge University Press.
- Khairoutdinov, M. F., & Kogan, Y. L. (1999). A large eddy simulation model with explicit microphysics: Validation against aircraft observations of a stratocumulus-topped boundary layer. *Journal of the atmospheric sciences*, 56(13), 2115–2131.
- Kohler, H. (1936). The nucleus in and the growth of hygroscopic droplets. *Transactions of the Faraday Society*, 32, 1152–1161.
- Kolb, C., Cox, R. A., Abbatt, J., Ammann, M., Davis, E., Donaldson, D., Garrett, B. C., George, C., Griffiths, P., Hanson, D., et al. (2010). An overview of current issues in the uptake of atmospheric trace gases by aerosols and clouds. *Atmospheric Chemistry and Physics*, 10(21), 10561–10605.
- Krueger, S. (2000). *Cloud system modelling*.
- Kumar, B., Bera, S., Prabha, T. V., & Grabowski, W. W. (2017). Cloud-edge mixing: Direct numerical simulation and observations in indian monsoon clouds. *Journal of Advances in Modeling Earth Systems*, 9, 332–353. <https://doi.org/10.1002/2016MS000731>

- Kumar, B., Götzfried, P., Suresh, N., Schumacher, J., & Shaw, R. A. (2018). Scale dependence of cloud microphysical response to turbulent entrainment and mixing. *Journal of Advances in Modeling Earth Systems*, 10(11), 2777–2785.
- Kuwata, M., Zorn, S. R., & Martin, S. T. (2012). Using elemental ratios to predict the density of organic material composed of carbon, hydrogen, and oxygen. *Environmental science & technology*, 46(2), 787–794.
- Lam, S. K., Pitrou, A., & Seibert, S. (2015). Numba: A llvm-based python jit compiler. *Proceedings of the Second Workshop on the LLVM Compiler Infrastructure in HPC*, 1–6.
- Lannuque, V., Camredon, M., Couvidat, F., Hodzic, A., Valorso, R., Madronich, S., Bessagnet, B., & Aumont, B. (2018). Exploration of the influence of environmental conditions on secondary organic aerosol formation and organic species properties using explicit simulations: Development of the vbs-gecko parameterization. *Atmospheric Chemistry and Physics*, 18(18), 13411–13428.
- Li, Y., Davidovits, P., Kolb, C., & Worsnop, D. (2001). Mass and thermal accommodation coefficients of h₂o (g) on liquid water as a function of temperature. *The Journal of Physical Chemistry A*, 105(47), 10627–10634.
- Lim, H. J., Carlton, A. G., & Turpin, B. J. (2005). Isoprene forms secondary organic aerosol through cloud processing: Model simulations. *Environmental Science and Technology*, 39, 4441–4446. <https://doi.org/10.1021/es048039h>
- Lindsey, D. T., & Fromm, M. (2008). Evidence of the cloud lifetime effect from wildfire-induced thunderstorms. *Geophysical Research Letters*, 35. <https://doi.org/10.1029/2008GL035680>
- Lowe, S. J., Partridge, D., Davies, J., Wilson, K., Topping, D., & Riipinen, I. (2019). Key drivers of cloud response to surface-active organics. *Nature communications*, 10(1), 5214.
- Lucas-Picher, P., Caya, D., Elia, R., & Laprise, R. (2008). Investigation of regional climate models' internal variability with a ten-member ensemble of 10-year simulations over a large domain. *Climate Dynamics*, 31, 927–940. <https://doi.org/10.1007/s00382-008-0384-8>
- MacMillan, T., Shaw, R. A., Cantrell, W. H., & Richter, D. H. (2022). Direct numerical simulation of turbulence and microphysics in the pi chamber. *Physical Review Fluids*, 7(2), 020501.
- Miles, R. E., Reid, J. P., & Riipinen, I. (2012). Comparison of approaches for measuring the mass accommodation coefficient for the condensation of water and sensitivities to uncertainties in thermophysical properties. *The Journal of Physical Chemistry A*, 116(44), 10810–10825.
- Milinski, S., Maher, N., & Olonscheck, D. (2020). How large does a large ensemble need to be? *Earth System Dynamics*, 11, 885–901. <https://doi.org/10.5194/esd-11-885-2020>

- Morrison, H., & Pinto, J. O. (2006). Intercomparison of bulk cloud microphysics schemes in mesoscale simulations of springtime arctic mixed-phase stratiform clouds. *Monthly weather review*, 134, 1880–1900.
- Morrison, H., van Lier-Walqui, M., Fridlind, A. M., Grabowski, W. W., Harrington, J. Y., Hoose, C., Korolev, A., Kumjian, M. R., Milbrandt, J. A., Pawlowska, H., Posselt, D. J., Prat, O. P., Reimel, K. J., Shima, S. I., van Diedenhoven, B., & Xue, L. (2020). Confronting the challenge of modeling cloud and precipitation microphysics. *Journal of Advances in Modeling Earth Systems*, 12. <https://doi.org/10.1029/2019MS001689>
- Ovadnevaite, J., Zuend, A., Laaksonen, A., Sanchez, K. J., Roberts, G., Ceburnis, D., Decesari, S., Rinaldi, M., Hodas, N., Facchini, M. C., Seinfeld, J. H., & O’Dowd, C. (2017). Surface tension prevails over solute effect in organic-influenced cloud droplet activation. *Nature*, 546, 637–641. <https://doi.org/10.1038/nature22806>
- Petters, M. D., & Kreidenweis, S. M. (2007). *Atmospheric chemistry and physics a single parameter representation of hygroscopic growth and cloud condensation nucleus activity*. www.atmos-chem-phys.net/7/1961/2007/
- Pruppacher, H. R., Klett, J. D., & Wang, P. K. (1998). Microphysics of clouds and precipitation.
- Raatikainen, T., Nenes, A., Seinfeld, J. H., Morales, R., Moore, R. H., Latham, T. L., Lance, S., Padró, L. T., Lin, J. J., Cerully, K. M., Bougiatioti, A., Cozic, J., Ruehl, C. R., Chuang, P. Y., Anderson, B. E., Flagan, R. C., Jonsson, H., Mihalopoulos, N., & Smith, J. N. (2013). Worldwide data sets constrain the water vapor uptake coefficient in cloud formation. *Proceedings of the National Academy of Sciences of the United States of America*, 110, 3760–3764. <https://doi.org/10.1073/pnas.1219591110>
- Randall, D., Khairoutdinov, M., Arakawa, A., & Grabowski, W. (2003). Breaking the cloud parameterization deadlock. *Bulletin of the American Meteorological Society*, 84(11), 1547–1564.
- Rastak, N., Pajunoja, A., Acosta Navarro, J. C., Ma, J., Song, M., Partridge, D. G., Kirkevåg, A., Leong, Y., Hu, W., Taylor, N., et al. (2017). Microphysical explanation of the rh-dependent water affinity of biogenic organic aerosol and its importance for climate. *Geophysical research letters*, 44(10), 5167–5177.
- Riener, N., Ault, A., West, M., Craig, R., & Curtis, J. (2019). Aerosol mixing state: Measurements, modeling, and impacts. *Reviews of Geophysics*, 57(2), 187–249.
- Riener, N., & West, M. (2013). Quantifying aerosol mixing state with entropy and diversity measures. *Atmospheric Chemistry and Physics*, 13(22), 11423–11439.
- Rogers, R. R., & Yau, M. K. (1989). *A short course in cloud physics*. Elsevier.
- Rossow, W. B. (1978). *Cloud microphysics: Analysis of the clouds of earth, venus, mars, and jupiter*.
- Rothenberg, D., & Wang, C. (2017). An aerosol activation metamodel of v1.2.0 of the pyrcel cloud parcel model: Development and offline assessment for use in an aerosol-climate

- model. *Geoscientific Model Development*, 10, 1817–1833. <https://doi.org/10.5194/gmd-10-1817-2017>
- Ruehl, C. R., Davies, J. F., & Wilson, K. R. (2016). *An interfacial mechanism for cloud droplet formation on organic aerosols*. <http://science.sciencemag.org/>
- Sageev, G., Flagan, R. C., Seinfeld, J. H., & Arnold, S. (1986). Condensation rate of water on aqueous droplets in the transition regime. *Journal of colloid and interface science*, 113(2), 421–429.
- Saleh, R., Donahue, N. M., & Robinson, A. L. (2013). Time scales for gas-particle partitioning equilibration of secondary organic aerosol formed from alpha-pinene ozonolysis. *Environmental Science and Technology*, 47, 5588–5594. <https://doi.org/10.1021/es400078d>
- Schmedding, R., & Zuend, A. (2023). A thermodynamic framework for bulk–surface partitioning in finite-volume mixed organic–inorganic aerosol particles and cloud droplets. *EGUsphere*, 1–42.
- Schneider, T., Teixeira, J., Bretherton, C. S., Brient, F., Pressel, K. G., Schär, C., & Siebesma, A. P. (2017). *Climate goals and computing the future of clouds*. <https://doi.org/10.1038/nclimate3190>
- Schnoor, J. L., et al. (1996). *Environmental modeling: Fate and transport of pollutants in water, air, and soil*. John Wiley; Sons.
- Seinfeld, J., & Pandis, S. (2016). *Atmospheric chemistry and physics: From air pollution to climate change*. Wiley.
- Shafir, U., & Gal-Chen, T. (1971). A numerical study of collision efficiencies and coalescence parameters for droplet pairs with radii up to 300 microns. *Journal of the Atmospheric Sciences*, 28, 741–751.
- Shaw, R. A. (2003). Particle-turbulence interactions in atmospheric clouds. *Annual Review of Fluid Mechanics*, 35(1), 183–227.
- Shaw, R. A., & Lamb, D. (1999). Experimental determination of the thermal accommodation and condensation coefficients of water. *The Journal of Chemical Physics*, 111(23), 10659–10663.
- Shima, S.-I., Kusano, K., Kawano, A., Sugiyama, T., & Kawahara, S. (2007). *Super-droplet method for the numerical simulation of clouds and precipitation: A particle-based microphysics model coupled with non-hydrostatic model*.
- Shiraiwa, M., Berkemeier, T., Schilling-Fahnestock, K., Seinfeld, J., & Pöschl, U. (2014). Molecular corridors and kinetic regimes in the multiphase chemical evolution of secondary organic aerosol. *Atmospheric Chemistry and Physics*, 14(16), 8323–8341.
- Shiraiwa, M., Pfrang, C., Koop, T., & Pöschl, U. (2012). Kinetic multi-layer model of gas-particle interactions in aerosols and clouds (km-gap): Linking condensation, evaporation and chemical reactions of organics, oxidants and water. *Atmospheric Chemistry and Physics*, 12(5), 2777–2794.

- Shiraiwa, M., Zuend, A., Bertram, A. K., & Seinfeld, J. H. (2013). Gas–particle partitioning of atmospheric aerosols: Interplay of physical state, non-ideal mixing and morphology. *Physical Chemistry Chemical Physics*, 15(27), 11441–11453.
- Siebert, H., & Shaw, R. A. (2017). Supersaturation fluctuations during the early stage of cumulus formation. *Journal of the Atmospheric Sciences*, 74(4), 975–988.
- Song, M., Marcolli, C., Krieger, U. K., Lienhard, D. M., & Peter, T. (2013). Morphologies of mixed organic/inorganic/aqueous aerosol droplets. *Faraday discussions*, 165, 289–316.
- Stolzenburg, D., Wang, M., Schervish, M., & Donahue, N. M. (2022). Tutorial: Dynamic organic growth modeling with a volatility basis set. *Journal of Aerosol Science*, 166. <https://doi.org/10.1016/j.jaerosci.2022.106063>
- The MathWorks, I. (2020). *Curve fitting toolbox*. Natick, Massachusetts, United State. <https://www.mathworks.com/products/curvefitting.html>
- Thomas, S., Ovchinnikov, M., Yang, F., van der Voort, D., Cantrell, W., Krueger, S. K., & Shaw, R. A. (2019). Scaling of an atmospheric model to simulate turbulence and cloud microphysics in the pi chamber. *Journal of Advances in Modeling Earth Systems*, 11(7), 1981–1994.
- Topping, D. (2022). Gas-to-particle partitioning. In D. Topping & M. Bane (Eds.), *Introduction to aerosol modelling: From theory to code* (pp. 32–75). John Wiley & Sons.
- Topping, D., & Bane, M. (2022). *Introduction to aerosol modelling: From theory to code*. John Wiley & Sons.
- Topping, D., Connolly, P., & Mcfiggans, G. (2013). Cloud droplet number enhanced by co-condensation of organic vapours. *Nature Geoscience*, 6, 443–446. <https://doi.org/10.1038/ngeo1809>
- Topping, D., McFiggans, G., Kiss, G., Z, V., M C, F., S, D., & M, M. (2007). *Surface tensions of multi-component mixed inorganic/organic aqueous systems of atmospheric significance: Measurements, model predictions and importance for cloud activation predictions*. www.atmos-chem-phys.net/7/2371/2007/
- Twomey, S. A., Pieprgrass, M., & Wolfe, T. L. (1984). An assessment of the impact of pollution on global cloud albedo. *Tellus*, 36 B, 356–366. <https://doi.org/10.1111/j.1600-0889.1984.tb00254.x>
- Vepsäläinen, S., Calderón, S. M., Malila, J., & Prisle, N. L. (2022). Comparison of six approaches to predicting droplet activation of surface active aerosol–part 1: Moderately surface active organics. *Atmospheric Chemistry and Physics*, 22(4), 2669–2687.
- Vesala, T., Kulmala, M., Rudolf, R., Vrtala, A., & Wagner, P. E. (1997). Models for condensational growth and evaporation of binary aerosol particles. *Journal of Aerosol Science*, 28(4), 565–598.
- Vieceli, J., Roeselová, M., & Tobias, D. J. (2004). Accommodation coefficients for water vapor at the air/water interface. *Chemical Physics Letters*, 393(1-3), 249–255.

- Wang, L. P., Rosa, B., Gao, H., He, G., & Jin, G. (2009). *Turbulent collision of inertial particles: Point-particle based, hybrid simulations and beyond*. <https://doi.org/10.1016/j.ijmultiphaseflow.2009.02.012>
- Wedi, N. P., Polichtchouk, I., Dueben, P., Anantharaj, V. G., Bauer, P., Boussetta, S., Browne, P., Deconinck, W., Gaudin, W., Hadade, I., et al. (2020). A baseline for global weather and climate simulations at 1 km resolution. *Journal of Advances in Modeling Earth Systems*, 12(11), e2020MS002192.
- Winkler, P. M., Vrtala, A., Wagner, P. E., Kulmala, M., Lehtinen, K. E., & Vesala, T. (2004). Mass and thermal accommodation during gas-liquid condensation of water. *Physical review letters*, 93(7), 075701.
- Winkler, P. (1973). The growth of atmospheric aerosol particles as a function of the relative humidity—ii. an improved concept of mixed nuclei. *Journal of Aerosol Science*, 4(5), 373–387.
- Zagaynov, V., Nuzhny, V., Cheusova, T., & Lushnikov, A. (2000). Evaporation of water droplet and condensation coefficient: Theory and experiment. *Journal of aerosol science*, 31, S795–S796.
- Zuend, A., Marcolli, C., Booth, A. M., Lienhard, D. M., Soonsin, V., Krieger, U. K., Topping, D., McFiggans, G., Peter, T., & Seinfeld, J. H. (2011). New and extended parameterization of the thermodynamic model aiomfac: Calculation of activity coefficients for organic-inorganic mixtures containing carboxyl, hydroxyl, carbonyl, ether, ester, alkenyl, alkyl, and aromatic functional groups. *Atmospheric Chemistry and Physics*, 11, 9155–9206. <https://doi.org/10.5194/acp-11-9155-2011>

8 Appendix

PARCELY USER GUIDE

Hello, and thank you for using PARCELY for your cloud parcel modelling needs. This document is a brief and informal instruction manual for first-time users. It will guide you on how to run the model, how to edit the main file to input your initial conditions, and explain the output file. The functions should be commented thoroughly enough that should you want to go looking around in there, it'll be clear what does what. For a theoretical explanation of the model and its physics (including equations and validations), I refer you to the “Model Description” file from my master’s thesis on the GitHub page.

The Main and Input File: PARCELY_MAIN.py

Domain Set-Up

```
1 # Total cubic centimeters of the domain (e.g 5cm3, 4.3cm3 etc.)
2 Cubes = 1
3 # Height of boundary box side (m)
4 BoxHeight = (Cubes**(1/3))*(1e-2)
5 # Setting a random generator seed for reproducibility
6 SeedNo = 1996
7 RNG = np.random.default_rng(SeedNo)
```

The variables are explained in the comments, but a word on SeedNo (short for seed number, set to the year of my birth by default because I’m an egomaniac) and RNG (short for random generator): If you want to run the model multiple times and want to keep the same aerosol distribution, **you must start from RNG**. Running the model without this line (say, selecting only from line 64 because all you did was change the run time) will result in numpy using a different generator (essentially a random one) and you won’t be using the same aerosol distribution.

Time Set-Up

```
1 # Initial timestep, seconds
2 dt = 0.000001
3 # Total model runtime, seconds
4 RunTime = 0.00001
5 # Number of evenly spaced time instances to save
6 M = 10
7 # Times of instances
```

```

8 Instances = np.arange(0, RunTime+RunTime/M, RunTime/M)
9 # Actually measured time instances
10 Time = np.zeros_like(Instances)
11 # Tolerance
12 mtol = 1e-23

```

If this is the first time running the model, I **strongly recommend running it first with these time settings**. This is due to possible compiling issues from the way the numba package works (imported in PARCELY_FUNCTIONS). Cached files will be missing, and thus the code needs to be compiled first. I have found that the most efficient way to compile is to run the model at these settings, and then once again, changing only RunTime to 10 seconds. Once you have done that, the model should be fully compiled and will run as fast as it can.

The time-step (dt) is an adaptive time-step (if it weren't I would still be running a simulation from September 2022) and so there should be no reason to change the initial value when performing basic runs of the model. The tolerance (mtol) is what limits the time-step size. As with most any adaptive solver you'll likely have to play around with the values, depending on your solute distribution. Distributions with smaller aerosols will require a high tolerance (I've settled on 10^{-23}) while a monotonic distribution with large radii can have a lower one (e.g. 10^{-21}). Be careful, *changing the tolerance will eventually alter your results*.

Organic Components Set-Up

```

1 # Surface tension calculation method
2 Modes = ['OrgFilm', 'Constant', 'MixRule', 'WaterTemp']
3 # Surface tension of pure water J/m^2
4 sft = 0.072
5 # Selected method
6 SurfMode = Modes[0]
7
8 # Total concentration (all phases)
9 # ug/m3
10 Scaling = 1
11 Concentrations = np.array([0.1, 0.1, 0.1, 0.12, 0.12, 0.12, 0.15,
12                             0.24, 0.48, 1.18])*Scaling
13
14 # Volatility/Saturation Concentration, ug/m3
15 LogVols = np.arange(-6, 4, 1, dtype=np.float64)
16 Cstar = 10.0**(LogVols)
17
18 # Organic parameters
19 # Surface tension
20 SurfTension = 0.04*np.ones(Concentrations.size)
21

```

```

22 EstimateParameters = False
23
24 if EstimateParameters is False:
25     # unitless
26     Kappas = np.ones(Concentrations.size)*0.1
27     # kg/m3
28     Densities = np.ones(Concentrations.size)*1400
29     # kg/mol
30     MoMass = np.linspace(400, 200, Concentrations.size)*1e-3
31
32 if EstimateParameters is True:
33     MoMass, Densities, Kappas = DF.MolecularCorridor(LogVols, RNG)
34
35 # OA parameter table
36 OAParameters = DF.OrganicsArray(MoMass, Concentrations, Kappas,
37                                  SurfTension, Densities, Cstar)

```

Here, you must first choose your selected mode. If you are running a bare-bones model with no organics whatsoever, you should select ‘Constant’ - meaning using the value for the surface tension of pure water (sft); this can be any value you choose, so it doesn’t have to be for pure water - or if you want to be more physically accurate, ‘WaterTemp’. ‘WaterTemp’ uses the surface tension of pure water but as a function of the ambient temperature. With organics, you can either select ‘MixRule’, which is simply a volume-weighted mixing rule for the surface tension, or ‘OrgFilm’, which solves for an organic film around the aerosol (you’re referred to the theoretical explanation if curious).

Scaling simply scales the concentration of organics (most likely to a smaller value) if needed. The concentrations, as mentioned in the comments, is what you’d like to have in total, not just gas-phase.

Surface tension, Kappas, Densities, and MoMass can easily be changed to have different values for each component, you don’t need to stick to the way it is here. As long as it in array-form (and the same length as Concentrations), you’re good.

EstimateParameters activates the molecular-corridor approximations if you don’t have specific values you want to use for the organic parameters. If you have exact values you want to use, keep it False.

Solute Set-Up

```

1 # Dirichlet mass fractions for non-monotone distribution
2 Dirichlet = False
3 # Allow organics
4 Organics = True
5 # Allow co-condensation

```

```

6 CoCond = True
7 # Allow distribution in kappa values
8 KappaRand = False
9
10 # Distribution type
11 Distribution = 'lognormal'
12
13 Ns = np.array([125, 65])*Cubes
14 Rs = np.array([0.011, 0.060])
15 Stds = np.array([1.2, 1.7])
16
17 Inorgs = np.array([[0],[0]])
18 InorgPopFrac = np.array([[100],[100]])
19 Orgs = [[0,1,2,3,4,5,6,7,8,9],[0,1,2,3,4,5,6,7,8,9]]
20
21 # If irrelevant, set to 0
22 PercCond = 0
23 MassFractions = [np.array(0.6, 0.1, 0.05, 0.05, 0.05, 0.05,
24                          0.03, 0.03, 0.02, 0.01, 0.01,)),
25                  np.array(0.6, 0.1, 0.05, 0.05, 0.05, 0.05,
26                          0.03, 0.03, 0.02, 0.01, 0.01,))]
27
28 # Number of droplets
29 NumberDrops = Ns.sum()
30
31 start = time.time()
32
33 # Get solute arrays
34 Solutes, SoluteFilter, VaporConcs = DF.SolPopInitialize(Ns, Rs, Stds,
35                                                         Inorgs, InorgPopPerc, Orgs,
36                                                         PercCond,
37                                                         OAParameters, RNG, MassFractions,
38                                                         Dirichlet, KappaRand, Organics,
39                                                         Cubes, Distribution)
40
41 # Get vapor concentrations
42 OAParameters[:,4] = VaporConcs
43
44 end = time.time()
45 print('Solute/OA Initialization: ', np.round(end - start, 4), 's')

```

This section is the last of the inputs (you're almost done!). After setting your preferences with the four Boolean inputs at the beginning, you must choose either a "mono", "normal", or "lognormal" Distribution (string). The example above is for an ammonium sulphate Pristine aerosol distribution, with the inorganic commanding 60% of the mass of each aerosol, and the rest taken up by the organic species. Each element in Ns/Rs/Std is a component of the

total distribution (one lognormal distribution with 125 particles, 0.011 geometric mean radius in μm , and geometric standard deviation in μm .)

For Inorgs, the integers indicate the index of the requested row from the INORGANICS CSV file. 0 is ammonium sulphate, in this example. This is an array of lists in order to allow for more freedom in determining which species are in which sub-distribution, and must be lists even if there's only one species per sub-distribution. The same goes for InorgPopPerc, which is the percentage of each species in each sub-distribution.

Orgs is a list of lists, where each list represents which organic species taken from the OAParameters table is present in condensed form in the aerosol sub-distributions.

PerCond is an alternative way to determine how much of each organic is in its condensed phase. I would stick with defining mass fractions though, as it is more straightforward. If you're persistent, PerCond takes an array of percentages indicating how much of the organic species has condensed.

MassFractions are fractions of each solute component (inorganic and organics) per sub-distribution. If Dirichlet is True, MassFractions is used as a set of parameters for a Dirichlet distribution, so that the solute mass fractions (inorganics, organics) are randomly distributed around the same proportions.

SolPopInitialize returns three things:

1. Solutes : array of your solute population (with or without organics)
2. SoluteFilter : array of your inorganic part of your solute (identical to Solutes if no organics present)
3. VaporConcs : If there are organics, this returns the vapor concentrations of the organics in $\mu\text{g m}^{-3}$ and are put into the organic parameters table on line 41. If no organics are involved, it returns 0.

That's it! The rest is automatic, and if you want to know what the functions in *Koehler Curves and Critical/Equilibrium parameters*, *Droplet Initialization*, and *Simulation* do, you can look into their descriptions.

The Output File

In keeping with the pure-Python style, the output file for PARCELY is a .npz file, which you can read about in a more technical manner [here](#). It is easily read into Python by the numpy load function, and consists of the following subfiles:

1. DropOutput - Array for the droplet data. In order, its columns are droplet index, position, vertical velocity, water mass, radius, surface saturation ratio, growth rate, and surface tension. First dimension is droplet, second is data column, third is time.
2. Solute - If co-condensation is included, this is an array similar to DropOutput but for the solute data instead. In order, its columns are solute index, radius, total solute mass, molar mass of inorganic, mean density, effective hygroscopicity, and the remainder are the organic mass of each component. Without co-condensation, the solute doesn't change with time so there is no time-dimension (2D array).
3. CritParams - 2D array of critical parameters assuming a surface tension of pure water. First column is critical radius, second is critical saturation ratio.
4. OAParams - If co-condensation is included, this output is the organic parameter array. Each row is a different organic component, and in order the columns are molar mass, density, diffusivity, saturation concentration, final vapor concentration, hygroscopicity, pure component surface tension, and total concentration.
5. ChemData - If co-condensation is included, this output is a 3D array where each column is an organic component, and the third dimension is time. The first dimension represents the data variables for each organic component, which are in order the vapor concentration in molecules per cubic centimeter, the saturation concentration in $\mu\text{g m}^{-3}$, the mean surface saturation concentration in $\mu\text{g m}^{-3}$, and the mean condensed mole fraction.
6. SatTime - The evolution of saturation ratio over time.
7. TempTime - The evolution of ambient temperature over time.
8. PressTime - The evolution of ambient pressure over time.
9. HeightTime - The mean height of the particles over time.
10. Time - Time array.
11. MontVars - Array containing the generator seed number, the updraft velocity, and the mass and thermal accommodation coefficients used in initializing the simulation.

To access one of the output subfiles, for example DropOutput:

```

1  # Load numpy
2  import numpy as np
3  # Load data file into memory
4  SimulationData = np.load('YourPathHere/DataFile.npz')
5  # Get droplet data
6  ExampleDropData = SimulationData['DropOutput']

```

Heterogeneous Extra

```
1      # By how much the air parcel's side is subdivided
2      SatDivide = 5
3      SatField, SatGrid, SatInd = DF.SatFieldInit(S, SatDivide,
4          DomainXLims, DomainYLims, DomainZLims, RNG, 'mono')
5
6      Diffusion = True
7      DropMove = True
8
9      TempField = np.ones_like(SatField)*T
10     PressField = np.ones_like(SatField)*P
```

In the heterogeneous version of PARCELY, where the domain is subdivided into a grid, we have this extra section above. In this example, SatDivide is set equal to 5, meaning we have 5 divisions per axis, resulting in 125 total sub-grids. Diffusion determines whether you allow the model to diffuse temperature and saturation ratio. DropMove allows the droplets to move with billiard-ball like motion in the horizontal (x,y directions).